Title: Perturbation of *de novo* lipogenesis hinders MERS-CoV assembly and release, but not the biogenesis of viral replication organelles.

Authors:

M. Soultsioti[1], A.W.M. de Jong[2], N. Blomberg[3], A. Tas[1], M. Giera[3], E. J. Snijder[1]#, M. Barcena[2] #

Affiliations:

1. Molecular Virology Laboratory, Center for Infectious Diseases (LUCID), Leiden University Medical Center
2. Section Electron Microscopy, Department of Cell and Chemical Biology, Leiden University Medical Center
3. Center for Proteomics and Metabolomics, Leiden University Medical Center

#Corresponding author: m.barcena@lumc.nl or e.j.snijder@lumc.nl

Keywords:

coronavirus, MERS-CoV, TOFA, acetyl-CoA carboxylase, lipid metabolism, viral assembly, replication organelles

Abstract (*max 250 words***)**

Coronaviruses hijack host cell metabolic pathways and resources to support their replication. They induce extensive host endomembrane remodeling to generate viral replication organelles, and exploit host membranes for assembly and budding of their enveloped progeny virions. Because of the overall significance of host membranes, we sought to gain insight into the role of host factors involved in lipid metabolism in cells infected with Middle East respiratory syndrome coronavirus

(MERS-CoV). We employed a single-cycle infection approach in combination with pharmacological inhibitors, biochemical assays, lipidomics, light and electron microscopy. Pharmacological inhibition of acetyl-CoA carboxylase (ACC) and fatty acid synthase (FASN), key host factors in *de novo* fatty acid biosynthesis, led to pronounced inhibition of MERS-CoV particle release. Inhibition of ACC led to a profound metabolic switch in Huh7 cells, altering their lipidomic profile and inducing lipolysis. However, despite the extensive changes induced by the ACC inhibitor, the biogenesis of viral replication organelles remained unaffected. Moreover, compound treatment triggered various simultaneous changes in the post-translational modifications of MERS-CoV envelope proteins, in addition to influencing their subcellular localization. Electron microscopy revealed an accumulation of nucleocapsids in early budding stages, indicating that MERS-CoV assembly is adversely impacted by ACC inhibition. Notably, inhibition of palmitoylation resulted in similar effects, while supplementation of exogenous palmitic acid reversed the compound's inhibitory effects, possibly reflecting a crucial need for palmitoylation of the MERS-CoV Spike and Envelope proteins for their role in virus particle assembly.

Importance (*max 150 words***)**

Middle East respiratory syndrome coronavirus (MERS-CoV) is the etiological agent of a zoonotic respiratory disease of limited transmissibility between humans. However, MERS-CoV is still considered a high-priority pathogen and is closely monitored by WHO due to its high lethality rate of around 35% of laboratory-confirmed infections. Like other positive-strand RNA viruses, MERS-CoV relies on the host cell's endomembranes to support various stages of its replication cycle. However, in spite of this general reliance of MERS-CoV replication on host cell lipid

metabolism, mechanistic insights are still very limited. In our study, we show that pharmacological inhibition of acetyl-CoA carboxylase (ACC), a key enzyme in the host cell's fatty acid biosynthesis pathway, significantly disrupts MERS-CoV particle assembly without exerting a negative effect on the biogenesis of viral replication organelles. Furthermore, our study highlights the potential of ACC as a target for the development of host-directed antiviral therapeutics against coronaviruses.

Introduction

Viruses rely heavily on the host cell's metabolic and biosynthetic capabilities to support their replication cycle. As such, the manipulation of host cell metabolic pathways has been a long-standing research topic for a range of evolutionary divergent DNA and RNA virus families, such as herpesviruses, flaviviruses, and picornaviruses, as reviewed in (1, 2). In the case of coronaviruses, virus-host interactions related to cellular metabolism constituted a rather poorly studied area until the emergence of severe acute respiratory syndrome coronavirus-2 (SARS-CoV-2) in December 2019 (3, 4). Since then, several studies have highlighted that coronaviruses, like other virus families, hijack host metabolic pathways to support various stages of their replication (5-12).

During their replication cycle (reviewed in (13-15)), coronaviruses, including the highly pathogenic SARS-CoV, SARS-CoV-2, and Middle East respiratory syndrome coronavirus (MERS-CoV), hijack intracellular membranes to accommodate viral RNA synthesis (16-23) and the assembly of enveloped progeny virions (21, 24-27). Briefly, after coronavirus entry and release of the positive-strand RNA genome (gRNA) into the cytoplasm, the gRNA is translated into two large replicase polyproteins that are autoproteolytically processed by internally encoded viral

proteases, resulting in the generation of 16 viral nonstructural proteins (nsps) that engage in viral RNA synthesis and a range of virus-host interactions. All coronaviruses studied so far induce the formation of a perinuclear network of modified membrane structures that derive from the endoplasmic reticulum (ER). This network includes double-membrane vesicles (DMVs), paired or convoluted membranes (CMs), and double-membrane spherules (DMSs), which are collectively referred to as the coronavirus replication organelle (RO) (18, 20). DMVs are the most abundant structures and constitute the primary site of viral genome replication and generation of subgenomic (sg) mRNAs (20, 21). A molecular pore complex was found to span the DMV membrane, thus connecting the DMV interior with the cytosol (28, 29) and presumably constituting a gateway for viral RNA export. In the cytoplasm, the sg mRNAs are translated, giving rise to the viral structural and accessory proteins. In parallel, part of the newly synthesized gRNAs associate with Nucleocapsid (N) proteins to form ribonucleoprotein (RNP) complexes, which constitute the nucleocapsid substructures that will be packaged in the virus particle. During their synthesis, the viral envelope proteins associate with membranes of the secretory pathway, into which the nucleocapsid buds. Progeny virions acquire their envelope from intracellular membranes that primarily originate from the ER-Golgi intermediate compartment (ERGIC) (21, 26), after which they are released from the infected cell. Historically, viral egress was thought to occur via the biosynthetic secretory pathway (30), but recent evidence suggests that coronaviruses may (also) employ parts of the lysosomal pathway (27, 31-33).

Given the overall significance of host cell lipids and membranes in pivotal stages of coronavirus replication, it is not surprising that recent genome-wide association studies (GWAS) have identified host factors involved in fatty acid biosynthesis/*de*

novo lipogenesis (DNL) and cholesterol biosynthesis to be important for the replication of SARS-CoV-2 and other coronaviruses (34-36). Host factors identified included the sterol regulatory element-binding proteins (SREBP-1 and SREBP-2) and SREBP cleavage-activating protein (SCAP), which are major regulators of DNL and cholesterol biosynthesis (37). A prior study also implicated SREBPs in MERS-CoV replication, potentially in DMV formation (6). Due to the impact of the SARS-CoV-2 pandemic and the urgency of developing broad-spectrum antiviral therapeutics, the potential of enzymes of the DNL pathway to serve as drug targets for intervention and treatment of COVID-19 has been explored, yielding some promising results (10, 38, 39). It should however be noted that, while most studies on coronavirus replication so far have uncovered a general reliance on DNL-related pathways, further mechanistic insights remain scarce.

The aim of our present study was to explore the role of DNL in the MERS-CoV replication cycle. Our results show that inhibition of acetyl-CoA carboxylase (ACC) disrupts the assembly of infectious MERS-CoV progeny, while the formation of viral replication organelles remains unaffected. The inhibitory effect on virus assembly could be partially reversed by supplementation with exogenous palmitic acid, possibly reflecting a need for palmitoylation of the MERS-CoV Spike (S) and Envelope (E) proteins. Our results also highlight the potential of ACC as a target for the development of host-directed antiviral treatment.

Results

MERS-CoV infection increases gene expression of host factors involved in DNL.

De novo lipogenesis begins with the generation of acetyl-CoA from citrate through the activity of ATP citrate lyase (ACLY) (Figure 1A). Acetyl-CoA is further carboxylated by the rate-limiting enzyme ACC, leading to the production of malonyl-CoA. Malonyl-CoA then serves as a substrate for the fatty acid synthase enzyme (FASN), leading to the generation of saturated fatty acids (such as myristic acid, palmitic acid, and stearic acid) that can be utilized in post-translational modifications (e.g., myristoylation and palmitoylation), phospholipid synthesis and fatty acid catabolism (β-oxidation) (Figure 1A).

First, we investigated if MERS-CoV infection altered the gene expression levels of various host factors involved in DNL (*ACLY, ACC, FASN, SCD-1*), phospholipid synthesis (*DGAT1*), formation of lipid droplets (LDs) (*ADRP*) or fatty acid oxidation pathways (*CPT1*α and *ACOX*). To this end, Huh7 cells were infected with MERS-CoV at a high multiplicity of infection (MOI 5). At 12 h p.i., cells were lysed and mRNA expression was analyzed by RT-qPCR. This timepoint was chosen as it combined abundant viral RNA synthesis with the early phase of virus assembly and release. Under such conditions, we observed an increase in the mRNA levels of host factors involved in initial steps of the DNL pathway such as the rate-limiting enzymes ACC and FASN, and an increase in the mRNA levels of ADRP (Figure 1B). From the fatty acid oxidation pathway factors that were analyzed, only ACOX was moderately increased. We then evaluated the expression of ACC and FASN on a protein level by Western blot analysis (Figure S1). Despite the observed alterations in mRNA levels, a clear change in the protein abundance of ACC and FASN could not be detected. However, this result may be attributed to the limited sensitivity of the assay or a reduced turn-over of these proteins.

Our observations overall suggested that host factors of the DNL branch of lipid metabolism are upregulated in MERS-CoV-infected cells.

DNL inhibition does not affect viral RNA synthesis but impairs a later step in the MERS-CoV replication cycle.

To investigate the role of DNL pathways in coronavirus replication, we made use of the fast-acting and potent small-molecule inhibitor 5-(tetradecyloxy)-2-furoic acid (TOFA), which blocks the activity of ACC and thus synthesis of fatty acids (Figure 1A) (40, 41). Our aim was to explore whether pharmacological inhibition of ACC would influence viral replication, in particular the steps that directly involve host cell endomembranes: replication organelle formation and assembly of progeny virions. For this, Huh7 cells were infected with MERS-CoV at MOI 5 and treated with non-cytotoxic concentrations of TOFA (Figure S2A) from 1 h p.i. onward, following removal of the virus inoculum. Total intracellular RNA and cell culture supernatant were collected at 16 h p.i. Interestingly, compared to the DMSO-treated control, no changes were observed in the levels of intracellular viral RNA (as detected by RT-qPCR) when infected Huh7 (Figure 2A) or MRC5 (Figure 2B) cells were treated with TOFA. However, by plaque assay we measured a 4-log reduction in infectious viral progeny released from Huh7 cells (Figure 2C) and an approximately 2.5-log reduction in the case of MRC5 cells (Figure 2D). When using TVB-2640, a small-molecule inhibitor that blocks the activity of FASN downstream of ACC (Figure 1A), similar trends were again observed in Huh7 cells, with the intracellular viral RNA levels remaining unaltered while the infectious progeny titers were reduced approximately 30-fold upon treatment (Figure 2E and 2F). Taken together, our data

indicated that the DNL branch of lipid metabolism plays a proviral role in MERS-CoV replication.

When MERS-CoV-infected Huh7 cells were treated with TOFA, the amount of infectious viral progeny was found to slowly increase from undetectable at 12 h p.i. to about 10^3 PFU/ml by 16 h p.i. Although the viral titers showed an increase over time, a systematic 4-log difference was observed when comparing the vehicle control and the TOFA-treated samples (Figure 2G). Overall, these data led us to conclude that pharmacological inhibition of ACC severely hampered virus assembly or egress, without affecting viral RNA synthesis.

Because of the significant reduction in extracellular infectious viral progeny following compound treatment, we sought to understand whether the pharmacological inhibition of ACC affected the host cell's secretory pathway, which is involved in virion release. Using a *Gaussia* luciferase reporter assay (42), we observed that TOFA did not affect the integrity of the secretory pathway, while Brefeldin A, a well-characterized protein trafficking inhibitor, strongly inhibited the secretion of *Gaussia* luciferase in the supernatant (Figure 2H). There were no differences in the intracellular levels of *Gaussia* luciferase across all conditions (Figure 2I), which excluded a general effect of TOFA on protein synthesis. Taken together, our data pointed to an intact secretory pathway in the TOFA-treated cells, without a negative, off-target effect of the compound on the cellular translation machinery, suggesting that the reduction in extracellular infectious particles was not due to a defective virus egress pathway.

TOFA alters the host cell lipidomic profile and induces lipolysis.

To gain insight into the phenotype of TOFA-treated Huh7 cells that might lead to the observed reduction in virus particle release (Figure 2G), uninfected cells were treated with the compound and harvested 12 h post treatment for targeted lipidomics analysis. This revealed that TOFA treatment induced profound changes in the host cell's lipidomic profile, including increased levels of phosphatidylcholine (Figure S3A), phosphatidylserine (S3B), lysophospholipids (Figure S3) and lipids of the ceramide biosynthetic pathway (Figure S3). Strikingly, the levels of neutral lipids including triacylglycerols (TG), cholesterol esters (CE) and diacylglycerols (DG) were significantly reduced (Figure 3A), while free fatty acids (FFA) increased. These latter effects strongly suggested a metabolic switch in TOFA-treated cells towards the hydrolysis of triacylglycerols into their constituent molecules of acylglycerols and cholesterol esters with a subsequent release of FFAs, a process also known as lipolysis. Lipolysis ultimately results in the degradation of LDs, which constitute the cellular neutral lipid storage compartments (43). To further investigate and validate these changes, we used BODIPY 493/503, a well-known neutral lipid dye, demonstrating a reduced accumulation of LDs compared to DMSO-treated control cells (Figure S3). Our results strongly suggested that pharmacological inhibition of ACC and thus FFA synthesis has a broader effect on lipid metabolism than previously described (41) and induces a shift toward lipolytic pathways as a compensation mechanism.

Similar effects could be observed in MERS-CoV-infected cells in a time-dependent manner, when they were treated with TOFA and fixed at 9 and 12 h p.i. The cells were then stained with BODIPY 493/503, and lipid droplets were imaged using immunofluorescence microscopy. At 9 h p.i., lipid droplets were still present at detectable levels in the TOFA-treated cells (Figure 3B, panel ii) although in

somewhat reduced amounts in comparison to the DMSO-treated control cells (Figure 3B, panel i). However, by 12 h p.i. there was a prominent difference between the DMSO- and TOFA-treated cells (Figure 3B, compare panels iii and iv), with LDs being strongly reduced in the latter.

Taken together, TOFA treatment appeared to induce a gradual metabolic rewiring towards lipolytic pathways in both mock-infected and MERS-CoV-infected cells.

The subcellular localization of MERS-CoV structural proteins is affected by ACC inhibition.

Next, we studied whether the trafficking of MERS-CoV envelope proteins was affected by ACC inhibition. To this end, we investigated their subcellular localization by immunofluorescence labeling and confocal microscopy, while using antibodies recognizing well-characterized host marker proteins to visualize specific compartments of the secretory pathway. Specifically, antibodies against S and M or S and E proteins were used for the simultaneous labeling of two of the envelope proteins, while in the same specimens antibodies against PDI, ERGIC-53, or giantin were used to stain the endoplasmic reticulum (ER), ER-Golgi intermediate compartment (ERGIC) and Golgi complex, respectively. As previously reported for other coronaviruses (26, 44, 45), in untreated infected cells, viral envelope proteins did not only co-localize in ERGIC (Figure S5), but also in Golgi membranes (Figure 4A-B). Interestingly however, after ACC inhibition, a change in the co-localization pattern of the envelope proteins was observed. Specifically, in the DMSO-treated control cells, the S protein co-localized with the giantin marker (white arrows, Figures 4A and 4B, panel i, yellow spots). Post-TOFA treatment, this co-localization pattern was not observed in the same intensity and the signal for both S and giantin proteins

seemed more dispersed (Figures 4A and 4B, panel ii). Subsequently, while in the untreated control cells S and E (Figure 4A) or S and M (Figure 4B) proteins co-localized with giantin (white arrows in Figures 4A and 4B, panel iii, white spots), the triple co-localization was not observed after TOFA treatment (Figures 4A and 4B, panel iv).

The loss of colocalization of S protein and giantin upon ACC inhibition potentially indicated an inhibition of viral envelope protein trafficking, as normally observed in MERS-CoV-infected cells.

TOFA treatment affects intracellular processing and trafficking of MERS-CoV envelope proteins.

Using Western blot, we further analyzed the status of the MERS-CoV structural proteins S, E, M and N extracellularly, in the culture supernatants of infected and TOFA-treated cells, as well as intracellularly.

Extracellularly, only trace amounts of the N protein could be detected in the supernatant collected from TOFA-treated infected cells (Figure 5A), while the amounts of the three envelope proteins were below the detection limit of our assay. Importantly, this result excluded the possibility that the decrease in viral infectivity titers in supernatants from TOFA-treated cells (Figure 2C) was merely due to the production of non-infectious virus particles.

Intracellularly, only the overall levels of N protein remained rather unaffected at 9 and 12 h p.i. Decreased levels of full-length (FL) S glycoprotein as well as its S1 and S2 fragments were observed, at 9 h and 12 h p.i. Moreover, after TOFA treatment, we could not detect a second band below the S2 fragment, which likely corresponds to the S2′ fragment (46), suggesting a decreased transport of the S protein to the

trans-Golgi network where the furin protease responsible for this cleavage is located. We also observed that the E protein consistently migrated slightly faster post-compound treatment, again suggesting changes in the protein's post-translational modifications (Figure 5B).

The M protein was detectable as the usual double band, indicative of the two different glycosylation states of M (47), migrating around 15-20 kDa (Figure 5B). However, following compound treatment, the blot for the M protein also revealed a smear of products with a higher molecular weight (in the 20-35 kDa range), suggesting a change in the post-translational maturation and/or trafficking of the M protein. The smear disappeared after glycosidase treatment of the cell lysates with PNGase (Figure 5C), confirming that it resulted from a change in the glycosylation status of M, which was likely linked to a disruption of the protein's intracellular trafficking.

Electron microscopy reveals that TOFA treatment interferes with MERS-CoV assembly and release.

Overall, our data confirmed that TOFA treatment caused a major defect in the release of infectious MERS-CoV progeny, and excluded the possibility that large amounts of non-infectious particles were secreted instead. Our subsequent microscopy and biochemical studies pointed towards changes in the post-translational modification and trafficking of all three MERS-CoV envelope proteins, which might disrupt the normal intracellular assembly of new virions.

To explore this possibility, we employed transmission electron microscopy (TEM) to gain a better insight into the impact of TOFA treatment on the viral replication cycle. Huh7 cells were infected with MERS-CoV at MOI 5 and treated with the compound

from 1 h p.i. onward. Cells were fixed at 12 h p.i. and analyzed with TEM. We observed that pharmacological inhibition of ACC did not affect the formation or morphology of virus-induced ROs (DMVs and CMs) in comparison to the vehicle-treated control cells (Figure 6A, panels i and ii), which aligns with our previous data regarding the unaffected intracellular viral RNA levels upon TOFA treatment (Figure 2A). Moreover, while extracellular progeny virions were abundantly found at the plasma membrane of untreated MERS-CoV-infected cells, they were hardly present in the TOFA-treated samples (Figure 6B, panels i. and ii.), which aligns with the strong reduction in progeny virus titers observed when ACC is inhibited (Figure 2B). Our ultrastructural studies further revealed that the effects of TOFA treatment hindered virus particle assembly. In untreated control samples (Figure 6C), different stages of virion budding could be detected, from early stages in which the nucleocapsid starts to be engulfed by a curved membrane (Figure 6C, panel i and ii) to (nearly) fully budded virions (panel iii), with the latter representing most virions. However, in TOFA-treated samples, the early stages of virus particle assembly were particularly abundant (Figure 6D), with exceptionally large areas containing particles representing this stage (Figure 6D, panels i and ii). This strongly suggested that TOFA treatment interferes with the normal progress towards a fully budded virus particle, leading to an unusual accumulation of nucleocapsids in an initial budding state.

Inhibition of palmitoyltransferase enzymes mimics the effects of ACC inhibition.

One of the many end products of the DNL pathway is the fatty acid palmitate. Palmitate, or palmitic acid, plays an important role in various cellular processes: as a

signaling molecule, a structural element of various lipids, and by participating in posttranslational modifications, such as protein palmitoylation catalyzed by palmitoyltransferase enzymes (48). Coronavirus S and E proteins contain a conserved C-terminal cysteine-rich region next to their transmembrane domain, which can serve as a palmitoylation substrate (Figure 7A) (49). Previous studies in cells infected with the murine hepatitis (MHV), transmissible gastroenteritis (TGEV), SARS-CoV and SARS-CoV-2 coronaviruses, have shown that their S proteins are post-translationally palmitoylated (50-57), while the cysteine-rich regions of the E proteins of SARS-CoV, MHV and infectious bronchitis virus (IBV) were also found to be palmitoylated (58-61). Since there is no experimental data on the palmitoylation status of the MERS-CoV S and E proteins and the potential role of this posttranslational modification in assembly, we initially tested the importance of palmitoyltransferase enzymes for MERS-CoV replication using 2-bromopalmitic acid (2-BP), a small-molecule inhibitor with a broad effect on palmitoyltransferase enzymes (Figure 1A) (62). A setup as previously described was used: Huh7 cells were infected with MOI 5, treated with 2-BP from 1 h p.i. onward and at 16 h p.i. culture supernatants and total intracellular RNA were collected. Interestingly, we observed that inhibition of palmitoyltransferase enzymes induced similar trends as the ACC inhibition (Figure 7B and 7C). Compared to the untreated control, no major changes were observed in the levels of intracellular viral RNA detected by RT-qPCR in cells treated with 2-BP (Figure 7B). However, there was a ~250-fold reduction in the extracellular infectious progeny titers (Figure 7C), aligning with the hypothesis that limited availability of palmitate after DNL inhibition may be partly responsible for the observed assembly impairment.

Addition of exogenous palmitic acid partially rescues assembly and release of MERS-CoV progeny.

Based on the possible involvement of palmitoylation defects in the observed disturbances of MERS-CoV assembly, we investigated whether assembly could be restored by supplementing some of the end products of the DNL pathway, such as palmitic acid or oleic acid. To this end, Huh7 cells were infected with MERS-CoV at MOI 5 and from 1 h p.i. onward they were treated with 10 μM TOFA or TOFA supplemented with 100 μM BSA-conjugated palmitic acid or BSA-conjugated oleic acid. A treatment with 100 μM BSA without conjugated fatty acid served as a vehicle control for the fatty acids (Figure 7D). Fatty acid concentrations where chosen based on previous cytotoxicity assays, using concentrations that would not reduce cell viability below 90% (Figures S2E and S2F), thus aiming to avoid potential confounding effects of lipotoxicity-induced cell death. Interestingly, we observed that the addition of exogenous palmitic acid conjugated with BSA partially restored the release of infectious MERS-CoV progeny in the supernatant (by almost 100-fold), while addition of BSA-conjugated oleic acid or BSA alone did not (Figure 7D). Moreover, the effects of TOFA treatment that we had observed at the level of individual envelope proteins (Figure 5) could be partially reversed by addition of palmitic acid, resulting in intracellular protein levels and post-translational modifications that were closer to those seen in samples from untreated infected cells (Figure 7E). Electron microscopy analysis of large EM data sets also revealed an increase in the number of extracellular virions after palmitic acid addition (Figure 7F), while intracellularly there was a significant decrease in the proportion of virions arrested in the early assembly stage (Figure 7G). In contrast, a quantitative analysis of the abundance of DMVs (Figure 7H) and CMs (Figure 7I) did not reveal significant

changes, neither due to the TOFA treatment in comparison to the DMSO control nor due to the addition of palmitic acid.

Overall, our data indicate an important role for palmitic acid during MERS-CoV assembly, potentially involving palmitoylation of the S and E structural proteins.

Discussion

Being enveloped positive-strand RNA viruses, coronaviruses depend on the host cell's endomembrane system to facilitate and support their propagation in several ways. They transform intracellular, ER-derived membranes into the ROs that accommodate viral RNA synthesis, and they hijack membranes of the secretory pathway to generate enveloped virus particles. Due to this extensive involvement of host membranes, lipid metabolism pathways have been implicated in coronavirus replication (5, 6). After the emergence of SARS-CoV-2, several studies touched upon the potential reprogramming of lipid metabolism in the context of coronaviral replication (8, 10, 11, 38), but few mechanistic details were resolved. Here, we report on the importance of lipid homeostasis in MERS-CoV-infected cells for viral propagation to take place, as perturbations of the fatty acid biosynthesis pathway were found to have a strong inhibitory effect, specifically on the assembly and/or release of viral progeny.

Due to the extensive remodeling of the ER during coronavirus RO biogenesis, it has been speculated that fatty acid biosynthetic pathways would be activated to fuel the formation of these membrane structures (6, 10). However, our data show that perturbation of DNL does not affect MERS-CoV RNA synthesis or RO biogenesis (Figure 2A, 2B, 2E and 6A), indicating that – contrary to previous speculations - DNL

is not among the host cell pathways critically required for coronaviral RO formation (6, 10).

Our data are in partial agreement with published literature on SARS-CoV-2. Earlier studies have shown that lipid metabolism pathways, especially anabolic branches such as DNL and not catabolism of fatty acids (like β-oxidation), play a general proviral role in coronavirus replication (6, 10, 38), which is also corroborated by our data when using inhibitors of ACC and FASN.

However, a previous immunofluorescence microscopy study of SARS-CoV-2-infected cells (10) showed that DNL inhibition leads to a change in the intracellular distribution of double-stranded RNA (dsRNA) foci, which was interpreted to represent a change in the formation of viral RO. In our study with MERS-CoV, such a dsRNA pattern change was not observed (Figure S8), while electron microscopy analyses of large EM data sets showed no alterations in the morphology (Figure 6) or abundance (Figure 7H-I) of viral ROs. The discrepancies could be attributed to technical immunolabeling differences or the use of different coronavirus species and host cells. Another technical difference in our study was the use of a single-cycle viral replication setup, in contrast to the multi-cycle approach and longer experimental timeframes applied in most of the previously published studies (6, 10, 38, 63). By using a single-cycle analysis, we tried to synchronize the different steps of the viral cycle (entry, RO formation, peak of viral RNA and protein synthesis, particle assembly) and study them at defined timepoints.

Our data indicate that the DNL pathway, and in particular palmitate, one of its end products, play a role in MERS-CoV particle assembly or maturation (Figure 7), instead of RO formation. Palmitoylation of the S and E proteins has been reported to be important for the replication of other coronaviruses, like MHV, SARS-CoV, and

SARS-CoV-2 (50-61), making it tempting to assume a similar involvement for MERS-CoV. However, palmitoylation of MERS-CoV structural proteins has not been investigated directly, in infected cells or overexpression/virus-like-particle systems. Consequently, the number of palmitoylated cysteines, and their role and position with respect to the transmembrane domain of the MERS-CoV S and E proteins remain unknown.

Depending on the coronavirus studied, disruption of palmitoylation seems to have divergent effects on the replication cycle. For example, palmitoylation of the MHV S protein seems to be necessary for its interaction with the M protein and assembly of virus particles (50), while palmitoylation of the SARS-CoV or SARS-CoV-2 S protein is not required for its interaction with the M protein (52, 54). It is unknown and rather difficult to predict what the importance of palmitoylation of the MERS-CoV envelope proteins might be, since the molecular interactions between coronaviral S and M protein are generally not well defined. In the coronaviruses studied so far, palmitoylation of S and E proteins seems to increase protein stability and to decrease their turnover rate (60, 61). This could also be the case for MERS-CoV, as suggested by the decrease we observed in intracellular S protein levels after ACC inhibition (Figure 5B). Attempts to use a triple-mutated MHV E protein lacking all potentially palmitoylated cysteines to generate virus-like particles (VLPs) or recombinant mutant MHV, resulted in particles incapable of proper assembly and release (60, 61) in both cases. Interestingly, this triple-mutated MHV E protein also exhibited faster migration during SDS-PAGE (60), which is in line with our western blot observations after ACC inhibition (Figure 5B) and the partial recovery of the protein's normal migration after addition of palmitic acid (Figure 7E). Besides impacting their stability, another common effect of palmitoylation on the S and E

proteins is the influence on their affinity for specific membrane lipid nanodomains (54, 60). Lack of S and E protein palmitoylation might lead to their association with membranes of different lipid composition than what is necessary for assembly, eventually leading to disruption of the regular assembly events. This is partially supported by our immunofluorescence microscopy data, since we observed reduced co-localization of the S and E proteins with a Golgi compartment marker (Figure 4).

The most abundant viral envelope protein and a key driver of particle assembly is the M protein, which has not been reported to be palmitoylated, but it is known to be glycosylated on its short N-terminal ectodomain. Upon TOFA treatment, the M protein exhibited differences in its glycosylation pattern (Figure 5B and 5C). Being on the luminal side of the membrane, the glycans decorating the MHV or SARS-CoV M proteins do not seem to have a crucial role in virion assembly and release, nor in M protein interactions with the S and E proteins (64, 65). However, these previous studies have mainly explored the use of mutated M proteins that lacked the specific amino acid residues normally used for glycan conjugation. In our study, following TOFA treatment, we observed M proteins carrying longer, possibly untrimmed, glycan chains. Trimming of glycan chains takes place as proteins progress from the ER to the Golgi complex, as part of the ER's quality control machinery for misfolded proteins. Glycans are further processed, trimmed, and extended during protein trafficking through the Golgi complex, as part of normal glycoprotein maturation (66, 67). Thus, the M protein's glycosylation differences observed in our study could signal trafficking issues that lead to delayed or improper processing of its (predicted) single N-linked glycan.

Although these changes may not affect virus assembly, they appear to support our immunofluorescence microscopy observations regarding the M protein's reduced

colocalization with giantin (Figure 4). According to the western blot results (Figure 5C), about half of the total amount of M protein still appears to be properly processed and trafficked, but the impact of the reduced or delayed availability of M protein at the site of virus assembly is difficult to predict.

In conclusion, the observed major impairment of the assembly and release of infectious MERS-CoV progeny upon ACC inhibition may well be a multifactorial phenomenon. In our TEM images (Figure 6D), inhibition of the fatty acid synthesis pathway resulted in a striking increase of the number of early assembly/budding events relative to (nearly) fully-formed virus particles. TOFA treatment may affect virus particle assembly by reducing palmitoylation of S and E proteins, which can potentially result in their instability and increased turnover. Simultaneous changes in M protein trafficking may contribute to an overall imbalance in the viral envelope proteins needed for interactions with each other, host lipids, and viral nucleocapsids, ultimately affecting the pace and quality of virion assembly and budding. In addition to its presumed impact on the trafficking and post-translational modification of viral envelope proteins, TOFA treatment may also affect the properties of unidentified host factors that are directly or indirectly involved in coronavirus assembly. This could also contribute to the general disruption of lipid metabolism pathways and the metabolic switch towards lipolytic pathways that we observed in both mock- and MERS-CoV-infected cells (Figure 3 and S3), which could contribute to an unfavorable microenvironment and host membrane composition for efficient virion assembly. The proviral role of *de novo* lipogenesis in MERS-CoV replication also highlights its potential as a target for the development of host-directed antiviral therapeutics against coronaviruses.

Materials and Methods

Cells

Huh7 cells (kindly provided by Dr. Ralf Bartenschlager, Heidelberg University, Germany) and MRC5 cells (purchased from ATCC, CCL-171) were cultured in Dulbecco's Modified Eagle Medium (DMEM) (Lonza) supplemented with 8% (v/v) fetal calf serum (FCS), 100 IU/mL penicillin/streptomycin, 2 mM L-glutamine, and non-essential amino acids, at 37°C and 5% CO_2.

Viruses and virus purification

MERS-CoV strain EMC/2012 (NC_019843) (68, 69) was kindly provided by Dr. Ron Fouchier, Erasmus Medical Center Rotterdam, the Netherlands, and working stocks were prepared using Huh7 cells. All work with live MERS-CoV was performed inside a biosafety level 3 facility at Leiden University Medical Center. Virus titrations by plaque assay were performed as described before (70). Huh7 cells were seeded in tissue culture-treated multiwell plates and the next day were infected with serial dilutions of MERS-CoV containing supernatant for 1 h at 37°C. The virus inoculum was removed and replaced by overlay medium containing 1.2% Avicel RC-581 (Cas. No.: 9004-34-6, FMC/IMCD Benelux) in DMEM supplemented with 2% FCS and 100 IU/mL penicillin/streptomycin. Cells were incubated for 3 days at 37°C, after which they were fixed with formaldehyde and stained with crystal violet.

Virus concentration by ultracentrifuge pelleting through a sucrose cushion (Figure 5A) was essentially carried out as previously described (71). Briefly, infected cell culture supernatants were harvested 16 h p.i. and clarified from cell debris by low-speed centrifugation at 1,200 g for 5 min at 4°C. The virus particles were pelleted through a 20% (w/v) sucrose cushion in TES buffer (0.02 M Tris-HCl, 1mM EDTA,

0.1 M NaCl, pH 7.4) by centrifugation in an SW41 Ti rotor (Beckman Coulter) for 3.5 h at 30,000 rpm and 4°C. Virus pellets were resuspended overnight in phosphate-buffered saline (PBS) at 4°C, lysed in 100mM Tris-HCl, pH 7.6 and 4% (w/v) sodium dodecyl sulfate (SDS), and used for SDS-PAGE and Western blot analysis.

Small-molecule inhibitors

TOFA (5-tetradecyloxy-2-furoic-acid, cat. No.: HY-101068) and TVB-2640 (Denifanstat, cat. No.: HY-112829) were purchased from MedChemExpress. 2-bromopalmitic acid (2-bromohexadecanoic acid, cat. No: 21604) was purchased from Sigma. Compounds were dissolved in anhydrous DMSO for stock preparation. BSA-conjugated palmitate saturated fatty acid complex (PA) (cat. No.: 29558), BSA-conjugated oleate monounsaturated fatty acid complex (OA) (cat. No. 29557) and BSA control for BSA-fatty acid complexes (cat. No. 29556) were purchased from Cayman Chemicals.

Cytotoxicity assays

Cell viability was monitored using CellTiter 96 aqueous non-radioactive cell proliferation reagent (Promega), following the manufacturer's instructions. Cells were seeded in 96-well plates and incubated overnight at 37°C and 5% CO2. On the next day, the cells were treated with serial dilutions of the different compounds in DMEM containing 2% FCS, 100 IU/mL penicillin/streptomycin, 2 mM L-glutamine and non-essential amino acids. Cells were incubated for 22 h, and then 20 ml/well of MTS solution (3-(4,5-dimethylthiazol-2-yl)-5-(3-carboxymethoxyphenyl)-2-(4-sulfophenyl)-2H-tetrazolium) were added. The cells were incubated for 2 h at 37°C, after which

the absorbance was measured at 495 nm using the Envision multiplate reader (PerkinElmer). Cell viability was normalized against the DMSO-treated control.

Quantitative PCR

Viral RNA in MERS-CoV-infected Huh7 cells was quantified by using RT-qPCR. To this end, samples were collected in Tripure Isolation Reagent (Sigma), intracellular RNA was isolated following the manufacturer's instructions, and RT-qPCR was performed using the TaqMan Fast Virus 1-step Multiplex Master Mix (ThermoFisher) with MERS-CoV-specific primers and probes described before (72) in a CFX384 Touch RT-PCR detection system (Biorad). For absolute quantification, a standard curve was generated using 10-fold serial dilutions of an *in vitro* transcript containing the target sequences, which was generated using T7 RNA polymerase.

Gene expression analysis for host factors was performed using real-time RT-qPCR with iTaq SYBR Green Supermix (Biorad) in a CFX384 Touch RT-PCR detection system (Biorad). Primer sequences for *ACLY, ACC, FASN, SCD-1, DGAT1, ADRP, CPT1a, ACOX* and human β-actin were described elsewhere (6, 73). Quantification was performed by normalizing against the amount of human β-actin mRNA. Fold gene expression changes in MERS-CoV-infected cells relative to mock-infected cells were calculated by using the delta-delta Ct formula ($2^{-\Delta\Delta Ct}$).

***Gaussia* luciferase reporter assay**

For monitoring the effect of TOFA on the secretory pathway's activity, Pierce™ *Gaussia* luciferase glow assay kit (ThermoFisher, cat. No.: 16160) was used following the manufacturer's instructions. Huh7 cells were seeded in 96-well plates and the next day, they were transfected with 150 ng of a Gaussia luciferase

expression plasmid using Lipofectamine 3000 (ThermoFisher) at a 1:3 ratio of DNA to Lipofectamine. At 24 h post transfection, the cell culture supernatant was aspirated, and the cells were treated for 8 h with DMSO, TOFA, or brefeldin A. After incubation with the compounds, the cell culture supernatant containing secreted *Gaussia* luciferase was collected, and the cell monolayer was lysed for detection of intracellular luciferase. The luciferase signal output was measured at 485 nm using an Envision multiplate reader (PerkinElmer).

Immunofluorescence microscopy

Huh7 cells were seeded on glass coverslips and left to attach overnight at 37°C and 5% CO2. The next day, cells were either mock- or MERS-CoV infected for 9 h or 12 h and then fixed with 3% paraformaldehyde. Immunofluorescence labelling was performed as described before (74). In this study, the following antibodies were used for immunofluorescence analyses: human monoclonal antibody against MERS-CoV Spike protein (kindly provided by Dr. Berend Jan Bosch, Utrecht University) (75), rabbit polyclonal anti-MERS-CoV M protein antibody (20, 76), rabbit polyclonal anti-MERS-CoV E protein antibody (ThermoFisher, cat. No.: PA5-143457), rabbit polyclonal anti MERS-CoV N protein antibody (Sino Biological, cat. No.: 40068-RP02), mouse monoclonal anti-dsRNA J2 antibody (Scicons), mouse monoclonal anti-PDI antibody (Enzo Life Sciences, ADI-SPA-891), mouse monoclonal ERGIC-53 G1/93 Ab (Enzo Life Sciences/ Alexis Biochemicals, ALX-804-602), mouse monoclonal anti-giantin antibody (Enzo Life Sciences/Alexis Biochemicals, ALX-804-600), BODIPY493/503 (ThermoFisher, cat. No.: D3922). For viral M and E protein labeling, an Alexa-647-conjugated donkey anti-rabbit secondary antibody (Jackson Laboratories, cat. No.: 711-605-152) was used, the S protein labelling was visualized

with an Alexa-488-conjugated goat anti-human antibody (ThermoFisher, cat. No.: A11013), while for the N protein labeling an Alexa-488-conjugated goat anti-rabbit secondary antibody (ThermoFisher, cat. No.: A11008) was used. Cellular organelle markers and dsRNA were labelled using a Cy3-conjugated donkey anti-mouse antibody (Jackson Laboratories, cat. No.: 715-165-150). Leica Sp8 confocal and DM6 fluorescence microscopes were used for image acquisition. For image processing, Leica Application Suite X version 3.7 software was used.

Targeted lipidomics analysis

Comprehensive, quantitative shotgun lipidomics was carried out as described in detail elsewhere (77, 78). Briefly, samples were spiked with deuterated internal standards and lipids were extracted using methyl tert-butyl ether. The combined organic extracts were subsequently dried under a gentle stream of nitrogen and the dried extracts were dissolved in methanol:chloroform 1:1 containing 10 mM ammonium acetate. Lipids were then analyzed with a flow injection method at a flow rate of 8 µL/min applying differential ion mobility for lipid class separation and subsequent multiple reaction monitoring in positive and negative electrospray ionization mode. Using the Shotgun Lipidomics Assistant (SLA) software individual lipid concentrations were calculated after correction for sample input and their respective internal standards.

Western blot and PNGase assay

After lysis of cells or purified virus particles, obtained as described above, the protein content of samples was quantified using the Pierce BCA protein assay kit (ThermoFisher). Samples were mixed with 4x Laemmli sample buffer, incubated at

96°C for 5 min, and separated using SDS-polyacrylamide gel electrophoresis (SDS-PAGE). Post separation, the proteins were transferred to Amersham Hybond-LFP 0.45 μm PVDF blotting membrane (Cytiva) using the semidry Trans-Blot Turbo Transfer System (Biorad). For the E protein, Amersham Hybond-LFP 0.2 μm PVDF blotting membrane was used instead. The membranes were blocked for 1 h at room temperature. For ACC and FASN, 5% bovine serum albumin (BSA) in TBS with 0.05% Tween-20 (TBST) was used as a blocking buffer, while for viral proteins 1% casein in PBS with 0.05% Tween-20 (PBST) was used instead. Membranes were incubated with primary antibodies overnight in 2.5% BSA in TBST or 0.5% casein in PBST respectively.

Antibodies used in this study were: ACC (Cell Signaling Technology, cat.no.: #3662), FASN (Cell Signaling Technology, cat.no.: #3180), rabbit polyclonal anti-MERS-CoV S1 antibody (ThermoFisher, cat. No.: PA5-119581), rabbit polyclonal anti-MERS-CoV S2 antibody (ThermoFisher, cat. No.: PA5-81788), rabbit polyclonal anti-MERS-CoV M protein antibody (20, 76), rabbit polyclonal anti-MERS-CoV E protein antibody (ThermoFisher, cat. No.: PA5-143457), rabbit polyclonal anti-MERS-CoV N protein antibody (Sino Biological, cat. No.: 40068-RP02), mouse monoclonal anti-β-actin antibody (Sigma, cat. No.: A5316). Following primary antibody incubation, membranes were incubated with a secondary antibody: biotin-conjugated anti-mouse IgG (Thermo Fisher Scientific, cat.no.: 31800) or anti-rabbit IgG (Thermo Fisher Scientific, cat.no.: A16033). After 1 h incubation at room temperature, the membranes were incubated for 1 h with a tertiary Cy3-conjugated anti-biotin antibody (Jackson Laboratories, cat.no.: 200-162-211). Protein bands were visualized using an Alliance Q9 advanced imaging system (Uvitec).

For the PNGase assay, the PNGase F kit (New England Biolabs, cat. no.: P0704) was used according to the manufacturer's instructions with a few modifications. The protocol for denaturing conditions was followed and the glycoprotein denaturing buffer was added directly to samples lysed with 4x Laemmli Sample Buffer. The samples were denatured by heating at 100°C for 10 min, they were briefly placed on ice and then centrifuged for 10 sec. GlycoBuffer, 10% NP-40 and H_2O were added to the denatured protein lysate according to NEB's protocol. The reaction mixture was incubated for 1 h at 37°C and then directly subjected to SDS-PAGE and Western blotting.

Electron microscopy

Cells were fixed with 1.5% (vol/vol) glutaraldehyde in 0.1 M cacodylate buffer (pH 7.4) for 30 min at room temperature, and then stored overnight at 4°C before being exported from the BSL3 facility. Then, the samples were first stained with OsO_4 at 4°C for 1 h and subsequently at room temperature with 1% (w/v) uranyl acetate in Milli-Q water for 1 h, with washing steps with 0.1 M cacodylate buffer in between. After a washing step with Milli-Q water, the samples were dehydrated in increasing concentrations of ethanol (70%, 80%, 90%, 100%), embedded in epoxy resin (LX-112, Ladd Research), and polymerized at 60°C. Sections were collected on mesh-100 copper EM grids covered with a carbon-coated Pioloform layer, and poststained with 7% (w/v) uranyl acetate and Reynold's lead citrate.

The samples were examined in a Tecnai12 BioTwin or a Twin transmission electron microscope, equipped with an Eagle 4k CCD camera (Thermo Fisher Scientific) or a OneView 4k high-frame rate CMOS camera (Gatan), respectively. For the quantifications, mosaic images of large areas were generated as described in (79),

with a pixel size of 2 nm. A minimum of 3 large mosaic images from at least 2 different EM grids were analyzed per condition, each one including ~10-25 cells and DMVs and virus particles were manually annotated and CM regions delineated using Aperio Imagescope software (Leica). On average, each of these large areas contained ~1,900 DMVs, as well as ~3,000 virus particles in different stages of assembly. The latter were classified based on their assembly stage: particles in early-stage assembly were defined as those with a budding envelope forming a crescent smaller than a semi-circle, whereas virus particles with a budding envelope forming a crescent larger than a semi-circle or appearing fully budded were assigned to the late-stage assembly class. The perimeter of cells and nuclei in these regions was also manually delineated to calculate densities per μm^2 of cytoplasm.

Statistical analysis

Data are represented as mean ± standard deviation (SD) of at least two biological replicates. Statistical significance was calculated using unpaired Student's t-test, when comparing two groups, or two-way ANOVA and applying multiple comparison corrections, when comparing multiple groups. Statistical significance is denoted with asterisks as: * $p<0.05$, ** $p< 0.01$, *** $p< 0.001$, **** $p< 0.0001$. Prism version 10 (GraphPad Software Inc.) was used to perform all statistical analyses and calculations.

Software

Geneious Software (version 10.2) was used for the alignment of partial S and E protein sequences from selected coronaviruses. The list of viruses was selected based on available information from published literature on S and E protein

palmitoylation modifications of these viruses. Their protein sequences were then compared to the sequences of MERS-CoV S and E proteins. The following accession numbers were used: MERS-CoV (NC_019843), SARS-CoV (NC_004718) SARS-CoV-2 (NC_045512), MHV (AY700211), TGEV (AJ271965), IBV (NC_001451), HCoV-229E (NC_001451).

Figure annotations (Fig. 5, 7E and S1) and schematics (Fig. 1A) were created using BioRender.com.

Supplementary data

Available with the main figures file.

Acknowledgements

The authors would like to thank Patrick Wanningen, Heidi de Gruyter, and Tim Dalebout for technical assistance, Annelies Boonzaier-van der Laan for confocal microscopy assistance, Nadya Urakova and Quinten Ducarmon for helpful discussions. The study was partially funded by the European Union's Horizon 2020 research and innovation program under the Marie Skłodowska-Curie grant agreement number 813343 (H2020-MSCA-ITN-813343-INITIATE), and by the Netherlands Organization for Scientific Research (grant NWO-OCENW.M.21.339).

Author Contribution

Study design, M.S., M.B., and E.J.S.; methodology, M.S., A.W.M.J., and N.B.; investigation, M.S., A.W.M.J., N.B., and A.T.; formal analysis, M.S. and M.B.; resources, M.G., M.B., and E.J.S.; writing – original draft, M.S., M.B., and E.J.S.;

writing - editing and final approval, M.S., A.W.M.J., A.T., N.B., M.G., M.B., and E.J.S.; supervision, M.B. and E.J.S.; funding acquisition, M.B. and E.J.S.

Conflict of Interest

The authors have no conflict of interest to declare.

References

1. Goodwin CM, Xu S, Munger J. 2015. Stealing the Keys to the Kitchen: Viral Manipulation of the Host Cell Metabolic Network. Trends in Microbiology 23:789-798.
2. Sanchez EL, Lagunoff M. 2015. Viral activation of cellular metabolism. Virology 479-480:609-618.
3. Zhou P, Yang X-L, Wang X-G, Hu B, Zhang L, Zhang W, Si H-R, Zhu Y, Li B, Huang C-L, Chen H-D, Chen J, Luo Y, Guo H, Jiang R-D, Liu M-Q, Chen Y, Shen X-R, Wang X, Zheng X-S, Zhao K, Chen Q-J, Deng F, Liu L-L, Yan B, Zhan F-X, Wang Y-Y, Xiao G-F, Shi Z-L. 2020. A pneumonia outbreak associated with a new coronavirus of probable bat origin. Nature 579:270-273.
4. Zhu N, Zhang D, Wang W, Li X, Yang B, Song J, Zhao X, Huang B, Shi W, Lu R, Niu P, Zhan F, Ma X, Wang D, Xu W, Wu G, Gao GF, Tan W. 2020. A Novel Coronavirus from Patients with Pneumonia in China, 2019. N Engl J Med 382:727-733.
5. Yan B, Chu H, Yang D, Sze K-H, Lai P-M, Yuan S, Shuai H, Wang Y, Kao RY-T, Chan JF-W, Yuen K-Y. 2019. Characterization of the Lipidomic Profile of Human Coronavirus-Infected Cells: Implications for Lipid Metabolism Remodeling upon Coronavirus Replication. Viruses 11:73.
6. Yuan S, Chu H, Chan JF-W, Ye Z-W, Wen L, Yan B, Lai P-M, Tee K-M, Huang J, Chen D, Li C, Zhao X, Yang D, Chiu MC, Yip C, Poon VK-M, Chan CC-S, Sze K-H, Zhou J, Chan IH-Y, Kok K-H, To KK-W, Kao RY-T, Lau JY-N, Jin D-Y, Perlman S, Yuen K-Y. 2019. SREBP-dependent lipidomic reprogramming as a broad-spectrum antiviral target. Nature Communications 10:120.
7. Codo AC, Davanzo GG, Monteiro LdB, de Souza GF, Muraro SP, Virgilio-da-Silva JV, Prodonoff JS, Carregari VC, de Biagi Junior CAO, Crunfli F, Jimenez Restrepo JL, Vendramini PH, Reis-de-Oliveira G, Bispo dos Santos K, Toledo-Teixeira DA, Parise PL, Martini MC, Marques RE, Carmo HR, Borin A, Coimbra LD, Boldrini VO, Brunetti NS, Vieira AS, Mansour E, Ulaf RG, Bernardes AF, Nunes TA, Ribeiro LC, Palma AC, Agrela MV, Moretti ML, Sposito AC, Pereira FB, Velloso LA, Vinolo MAR, Damasio A, Proença-Módena JL, Carvalho RF, Mori MA, Martins-de-Souza D, Nakaya HI, Farias AS, Moraes-Vieira PM. 2020. Elevated Glucose Levels Favor SARS-CoV-2 Infection and Monocyte Response through a HIF-1α/Glycolysis-Dependent Axis. Cell Metabolism 32:437-446.e5.
8. Dias SSG, Soares VC, Ferreira AC, Sacramento CQ, Fintelman-Rodrigues N, Temerozo JR, Teixeira L, Nunes da Silva MA, Barreto E, Mattos M, de Freitas CS, Azevedo-Quintanilha IG, Manso PPA, Miranda MD, Siqueira MM, Hottz ED, Pao CRR, Bou-Habib DC, Barreto-Vieira DF, Bozza FA, Souza TML, Bozza PT. 2020. Lipid droplets fuel SARS-CoV-2 replication and production of inflammatory mediators. PLoS Pathog 16:e1009127.
9. Zhang Y, Guo R, Kim SH, Shah H, Zhang S, Liang JH, Fang Y, Gentili M, Leary CNO, Elledge SJ, Hung DT, Mootha VK, Gewurz BE. 2021. SARS-CoV-2 hijacks folate and one-carbon metabolism for viral replication. Nature Communications 12:1676.

761 10. Williams CG, Jureka AS, Silvas JA, Nicolini AM, Chvatal SA, Carlson-Stevermer J, Oki J, Holden
762 K, Basler CF. 2021. Inhibitors of VPS34 and fatty-acid metabolism suppress SARS-CoV-2
763 replication. Cell Rep 36:109479.
764 11. Farley SE, Kyle JE, Leier HC, Bramer LM, Weinstein JB, Bates TA, Lee J-Y, Metz TO, Schultz C,
765 Tafesse FG. 2022. A global lipid map reveals host dependency factors conserved across
766 SARS-CoV-2 variants. Nature Communications 13:3487.
767 12. Greene KS, Choi A, Chen M, Yang N, Li R, Qiu Y, Lukey MJ, Rojas KS, Shen J, Wilson KF, Katt
768 WP, Whittaker GR, Cerione RA. 2023. Inhibiting Glutamine Metabolism Blocks Coronavirus
769 Replication in Mammalian Cells. bioRxiv
770 doi:10.1101/2023.09.27.559756:2023.09.27.559756.
771 13. Wang Y, Grunewald M, Perlman S. 2020. Coronaviruses: An Updated Overview of Their
772 Replication and Pathogenesis, p 1-29. *In* Maier HJ, Bickerton E (ed), Coronaviruses: Methods
773 and Protocols doi:10.1007/978-1-0716-0900-2_1. Springer US, New York, NY.
774 14. Malone B, Urakova N, Snijder EJ, Campbell EA. 2022. Structures and functions of coronavirus
775 replication-transcription complexes and their relevance for SARS-CoV-2 drug design. Nat Rev
776 Mol Cell Biol 23:21-39.
777 15. Steiner S, Kratzel A, Barut GT, Lang RM, Aguiar Moreira E, Thomann L, Kelly JN, Thiel V. 2024.
778 SARS-CoV-2 biology and host interactions. Nat Rev Microbiol doi:10.1038/s41579-023-
779 01003-z.
780 16. Gosert R, Kanjanahaluethai A, Egger D, Bienz K, Baker SC. 2002. RNA replication of mouse
781 hepatitis virus takes place at double-membrane vesicles. J Virol 76:3697-708.
782 17. Snijder EJ, van der Meer Y, Zevenhoven-Dobbe J, Onderwater JJ, van der Meulen J, Koerten
783 HK, Mommaas AM. 2006. Ultrastructure and origin of membrane vesicles associated with
784 the severe acute respiratory syndrome coronavirus replication complex. J Virol 80:5927-40.
785 18. Knoops K, Kikkert M, Worm SHEVD, Zevenhoven-Dobbe JC, Van Der Meer Y, Koster AJ,
786 Mommaas AM, Snijder EJ. 2008. SARS-Coronavirus Replication Is Supported by a
787 Reticulovesicular Network of Modified Endoplasmic Reticulum. PLoS Biology 6:e226.
788 19. Maier HJ, Neuman BW, Bickerton E, Keep SM, Alrashedi H, Hall R, Britton P. 2016. Extensive
789 coronavirus-induced membrane rearrangements are not a determinant of pathogenicity.
790 Scientific Reports 6:27126.
791 20. Snijder EJ, Limpens RWAL, De Wilde AH, De Jong AWM, Zevenhoven-Dobbe JC, Maier HJ,
792 Faas FFGA, Koster AJ, Bárcena M. 2020. A unifying structural and functional model of the
793 coronavirus replication organelle: Tracking down RNA synthesis. PLOS Biology 18:e3000715.
794 21. Klein S, Cortese M, Winter SL, Wachsmuth-Melm M, Neufeldt CJ, Cerikan B, Stanifer ML,
795 Boulant S, Bartenschlager R, Chlanda P. 2020. SARS-CoV-2 structure and replication
796 characterized by in situ cryo-electron tomography. Nature Communications 11:5885.
797 22. Cortese M, Lee J-Y, Cerikan B, Neufeldt CJ, Oorschot VMJ, Köhrer S, Hennies J, Schieber NL,
798 Ronchi P, Mizzon G, Romero-Brey I, Santarella-Mellwig R, Schorb M, Boermel M, Mocaer K,
799 Beckwith MS, Templin RM, Gross V, Pape C, Tischer C, Frankish J, Horvat NK, Laketa V,
800 Stanifer M, Boulant S, Ruggieri A, Chatel-Chaix L, Schwab Y, Bartenschlager R. 2020.
801 Integrative Imaging Reveals SARS-CoV-2-Induced Reshaping of Subcellular Morphologies.
802 Cell Host & Microbe 28:853-866.e5.
803 23. Ogando NS, Dalebout TJ, Zevenhoven-Dobbe JC, Limpens R, van der Meer Y, Caly L, Druce J,
804 de Vries JJC, Kikkert M, Bárcena M, Sidorov I, Snijder EJ. 2020. SARS-coronavirus-2
805 replication in Vero E6 cells: replication kinetics, rapid adaptation and cytopathology. J Gen
806 Virol 101:925-940.
807 24. Tooze J, Tooze S, Warren G. 1984. Replication of coronavirus MHV-A59 in sac- cells:
808 determination of the first site of budding of progeny virions. Eur J Cell Biol 33:281-93.
809 25. Klumperman J, Locker JK, Meijer A, Horzinek MC, Geuze HJ, Rottier PJ. 1994. Coronavirus M
810 proteins accumulate in the Golgi complex beyond the site of virion budding. Journal of
811 Virology 68:6523-6534.

812 26. Stertz S, Reichelt M, Spiegel M, Kuri T, Martínez-Sobrido L, García-Sastre A, Weber F, Kochs
813 G. 2007. The intracellular sites of early replication and budding of SARS-coronavirus. Virology
814 361:304-315.
815 27. Ghosh S, Dellibovi-Ragheb TA, Kerviel A, Pak E, Qiu Q, Fisher M, Takvorian PM, Bleck C, Hsu
816 VW, Fehr AR, Perlman S, Achar SR, Straus MR, Whittaker GR, de Haan CAM, Kehrl J, Altan-
817 Bonnet G, Altan-Bonnet N. 2020. β-Coronaviruses Use Lysosomes for Egress Instead of the
818 Biosynthetic Secretory Pathway. Cell 183:1520-1535.e14.
819 28. Wolff G, Limpens R, Zevenhoven-Dobbe JC, Laugks U, Zheng S, de Jong AWM, Koning RI,
820 Agard DA, Grünewald K, Koster AJ, Snijder EJ, Bárcena M. 2020. A molecular pore spans the
821 double membrane of the coronavirus replication organelle. Science 369:1395-1398.
822 29. Zimmermann L, Zhao X, Makroczyova J, Wachsmuth-Melm M, Prasad V, Hensel Z,
823 Bartenschlager R, Chlanda P. 2023. SARS-CoV-2 nsp3 and nsp4 are minimal constituents of a
824 pore spanning replication organelle. Nature Communications 14:7894.
825 30. Tooze J, Tooze SA, Fuller SD. 1987. Sorting of progeny coronavirus from condensed secretory
826 proteins at the exit from the trans-Golgi network of AtT20 cells. J Cell Biol 105:1215-26.
827 31. Scherer KM, Mascheroni L, Carnell GW, Wunderlich LCS, Makarchuk S, Brockhoff M, Mela I,
828 Fernandez-Villegas A, Barysevich M, Stewart H, Suau Sans M, George CL, Lamb JR, Kaminski-
829 Schierle GS, Heeney JL, Kaminski CF. 2022. SARS-CoV-2 nucleocapsid protein adheres to
830 replication organelles before viral assembly at the Golgi/ERGIC and lysosome-mediated
831 egress. Science Advances 8:eabl4895.
832 32. Miura K, Suzuki Y, Ishida K, Arakawa M, Wu H, Fujioka Y, Emi A, Maeda K, Hamajima R,
833 Nakano T, Tenno T, Hiroaki H, Morita E. 2023. Distinct motifs in the E protein are required
834 for SARS-CoV-2 virus particle formation and lysosomal deacidification in host cells. J Virol
835 97:e0042623.
836 33. Pearson GJ, Mears HV, Broncel M, Snijders AP, Bauer DLV, Carlton JG. 2024. ER-export and
837 ARFRP1/AP-1-dependent delivery of SARS-CoV-2 Envelope to lysosomes controls late stages
838 of viral replication. Sci Adv 10:eadl5012.
839 34. Daniloski Z, Jordan TX, Wessels HH, Hoagland DA, Kasela S, Legut M, Maniatis S, Mimitou EP,
840 Lu L, Geller E, Danziger O, Rosenberg BR, Phatnani H, Smibert P, Lappalainen T, tenOever BR,
841 Sanjana NE. 2021. Identification of Required Host Factors for SARS-CoV-2 Infection in Human
842 Cells. Cell 184:92-105.e16.
843 35. Wang R, Simoneau CR, Kulsuptrakul J, Bouhaddou M, Travisano KA, Hayashi JM, Carlson-
844 Stevermer J, Zengel JR, Richards CM, Fozouni P, Oki J, Rodriguez L, Joehnk B, Walcott K,
845 Holden K, Sil A, Carette JE, Krogan NJ, Ott M, Puschnik AS. 2021. Genetic Screens Identify
846 Host Factors for SARS-CoV-2 and Common Cold Coronaviruses. Cell 184:106-119.e14.
847 36. Schneider WM, Luna JM, Hoffmann HH, Sánchez-Rivera FJ, Leal AA, Ashbrook AW, Le Pen J,
848 Ricardo-Lax I, Michailidis E, Peace A, Stenzel AF, Lowe SW, MacDonald MR, Rice CM, Poirier
849 JT. 2021. Genome-Scale Identification of SARS-CoV-2 and Pan-coronavirus Host Factor
850 Networks. Cell 184:120-132.e14.
851 37. Eberlé D, Hegarty B, Bossard P, Ferré P, Foufelle F. 2004. SREBP transcription factors: master
852 regulators of lipid homeostasis. Biochimie 86:839-848.
853 38. Chu J, Xing C, Du Y, Duan T, Liu S, Zhang P, Cheng C, Henley J, Liu X, Qian C, Yin B, Wang HY,
854 Wang RF. 2021. Pharmacological inhibition of fatty acid synthesis blocks SARS-CoV-2
855 replication. Nat Metab 3:1466-1475.
856 39. Duan X, Tang X, Nair MS, Zhang T, Qiu Y, Zhang W, Wang P, Huang Y, Xiang J, Wang H,
857 Schwartz RE, Ho DD, Evans T, Chen S. 2021. An airway organoid-based screen identifies a
858 role for the HIF1α-glycolysis axis in SARS-CoV-2 infection. Cell Reports 37:109920.
859 40. McCune SA, Harris RA. 1979. Mechanism responsible for 5-(tetradecyloxy)-2-furoic acid
860 inhibition of hepatic lipogenesis. J Biol Chem 254:10095-101.
861 41. Halvorson DL, McCune SA. 1984. Inhibition of fatty acid synthesis in isolated adipocytes by 5-
862 (tetradecyloxy)-2-furoic acid. Lipids 19:851-6.

863 42. Tannous BA. 2009. Gaussia luciferase reporter assay for monitoring biological processes in
864 culture and in vivo. Nat Protoc 4:582-91.
865 43. Grabner GF, Xie H, Schweiger M, Zechner R. 2021. Lipolysis: cellular mechanisms for lipid
866 mobilization from fat stores. Nature Metabolism 3:1445-1465.
867 44. Lim KP, Liu DX. 2001. The Missing Link in Coronavirus Assembly: Retention of the avian
868 coronavirus infectious bronchitis virus envelope protein in the pre-Golgi compartments and
869 physical interaction between the envelope and membrane proteins. Journal of Biological
870 Chemistry 276:17515-17523.
871 45. Venkatagopalan P, Daskalova SM, Lopez LA, Dolezal KA, Hogue BG. 2015. Coronavirus
872 envelope (E) protein remains at the site of assembly. Virology 478:75-85.
873 46. Millet JK, Whittaker GR. 2014. Host cell entry of Middle East respiratory syndrome
874 coronavirus after two-step, furin-mediated activation of the spike protein. Proceedings of
875 the National Academy of Sciences 111:15214-15219.
876 47. Perrier A, Bonnin A, Desmarets L, Danneels A, Goffard A, Rouille Y, Dubuisson J, Belouzard S.
877 2019. The C-terminal domain of the MERS coronavirus M protein contains a trans-Golgi
878 network localization signal. J Biol Chem 294:14406-14421.
879 48. F SM, Abrami L, Linder ME, Bamji SX, Dickinson BC, van der Goot FG. 2024. Mechanisms and
880 functions of protein S-acylation. Nat Rev Mol Cell Biol 25:488-509.
881 49. J Alsaadi EA, Jones IM. 2019. Membrane Binding Proteins of Coronaviruses. Future Virology
882 14:275-286.
883 50. Thorp EB, Boscarino JA, Logan HL, Goletz JT, Gallagher TM. 2006. Palmitoylations on murine
884 coronavirus spike proteins are essential for virion assembly and infectivity. J Virol 80:1280-9.
885 51. Petit CM, Chouljenko VN, Iyer A, Colgrove R, Farzan M, Knipe DM, Kousoulas KG. 2007.
886 Palmitoylation of the cysteine-rich endodomain of the SARS-coronavirus spike glycoprotein
887 is important for spike-mediated cell fusion. Virology 360:264-74.
888 52. McBride CE, Machamer CE. 2010. Palmitoylation of SARS-CoV S protein is necessary for
889 partitioning into detergent-resistant membranes and cell-cell fusion but not interaction with
890 M protein. Virology 405:139-48.
891 53. Gelhaus S, Thaa B, Eschke K, Veit M, Schwegmann-Wessels C. 2014. Palmitoylation of the
892 Alphacoronavirus TGEV spike protein S is essential for incorporation into virus-like particles
893 but dispensable for S-M interaction. Virology 464-465:397-405.
894 54. Mesquita FS, Abrami L, Sergeeva O, Turelli P, Qing E, Kunz B, Raclot C, Paz Montoya J,
895 Abriata LA, Gallagher T, Dal Peraro M, Trono D, D'Angelo G, van der Goot FG. 2021. S-
896 acylation controls SARS-CoV-2 membrane lipid organization and enhances infectivity. Dev
897 Cell 56:2790-2807 e8.
898 55. Wu Z, Zhang Z, Wang X, Zhang J, Ren C, Li Y, Gao L, Liang X, Wang P, Ma C. 2021.
899 Palmitoylation of SARS-CoV-2 S protein is essential for viral infectivity. Signal Transduct
900 Target Ther 6:231.
901 56. Puthenveetil R, Lun CM, Murphy RE, Healy LB, Vilmen G, Christenson ET, Freed EO, Banerjee
902 A. 2021. S-acylation of SARS-CoV-2 spike protein: Mechanistic dissection, in vitro
903 reconstitution and role in viral infectivity. J Biol Chem 297:101112.
904 57. Li D, Liu Y, Lu Y, Gao S, Zhang L. 2022. Palmitoylation of SARS-CoV-2 S protein is critical for S-
905 mediated syncytia formation and virus entry. J Med Virol 94:342-348.
906 58. Corse E, Machamer Carolyn E. 2002. The Cytoplasmic Tail of Infectious Bronchitis Virus E
907 Protein Directs Golgi Targeting. Journal of Virology 76:1273-1284.
908 59. Liao Y, Yuan Q, Torres J, Tam JP, Liu DX. 2006. Biochemical and functional characterization of
909 the membrane association and membrane permeabilizing activity of the severe acute
910 respiratory syndrome coronavirus envelope protein. Virology 349:264-75.
911 60. Boscarino JA, Logan HL, Lacny JJ, Gallagher TM. 2008. Envelope protein palmitoylations are
912 crucial for murine coronavirus assembly. J Virol 82:2989-99.

913 61. Lopez Lisa A, Riffle Ambere J, Pike Steven L, Gardner D, Hogue Brenda G. 2008. Importance
914 of Conserved Cysteine Residues in the Coronavirus Envelope Protein. Journal of Virology
915 82:3000-3010.
916 62. Webb Y, Hermida-Matsumoto L, Resh MD. 2000. Inhibition of protein palmitoylation, raft
917 localization, and T cell signaling by 2-bromopalmitate and polyunsaturated fatty acids. J Biol
918 Chem 275:261-70.
919 63. Yuan S, Yan B, Cao J, Ye Z-W, Liang R, Tang K, Luo C, Cai J, Chu H, Chung TW-H, To KK-W,
920 Hung IF-N, Jin D-Y, Chan JF-W, Yuen K-Y. 2021. SARS-CoV-2 exploits host DGAT and ADRP for
921 efficient replication. Cell Discovery 7:100.
922 64. de Haan CA, Kuo L, Masters PS, Vennema H, Rottier PJ. 1998. Coronavirus particle assembly:
923 primary structure requirements of the membrane protein. J Virol 72:6838-50.
924 65. de Haan CA, Smeets M, Vernooij F, Vennema H, Rottier PJ. 1999. Mapping of the coronavirus
925 membrane protein domains involved in interaction with the spike protein. J Virol 73:7441-
926 52.
927 66. Helenius A, Aebi M. 2004. Roles of N-linked glycans in the endoplasmic reticulum. Annu Rev
928 Biochem 73:1019-49.
929 67. Moremen KW, Tiemeyer M, Nairn AV. 2012. Vertebrate protein glycosylation: diversity,
930 synthesis and function. Nat Rev Mol Cell Biol 13:448-62.
931 68. van Boheemen S, de Graaf M, Lauber C, Bestebroer Theo M, Raj VS, Zaki Ali M, Osterhaus
932 Albert DME, Haagmans Bart L, Gorbalenya Alexander E, Snijder Eric J, Fouchier Ron AM.
933 2012. Genomic Characterization of a Newly Discovered Coronavirus Associated with Acute
934 Respiratory Distress Syndrome in Humans. mBio 3:e00473-12.
935 69. Zaki AM, van Boheemen S, Bestebroer TM, Osterhaus AD, Fouchier RA. 2012. Isolation of a
936 novel coronavirus from a man with pneumonia in Saudi Arabia. N Engl J Med 367:1814-20.
937 70. van den Worm SH, Eriksson KK, Zevenhoven JC, Weber F, Züst R, Kuri T, Dijkman R, Chang G,
938 Siddell SG, Snijder EJ, Thiel V, Davidson AD. 2012. Reverse genetics of SARS-related
939 coronavirus using vaccinia virus-based recombination. PLoS One 7:e32857.
940 71. Wieringa R, de Vries AA, van der Meulen J, Godeke GJ, Onderwater JJ, van Tol H, Koerten HK,
941 Mommaas AM, Snijder EJ, Rottier PJ. 2004. Structural protein requirements in equine
942 arteritis virus assembly. J Virol 78:13019-27.
943 72. Ogando NS, Zevenhoven-Dobbe JC, Meer Yvd, Bredenbeek PJ, Posthuma CC, Snijder EJ.
944 2020. The Enzymatic Activity of the nsp14 Exoribonuclease Is Critical for Replication of
945 MERS-CoV and SARS-CoV-2. Journal of Virology 94:10.1128/jvi.01246-20.
946 73. van Huizen M, Bloeme - ter Horst JR, de Gruyter HLM, Geurink PP, van der Heden van Noort
947 GJ, Knaap RCM, Nelemans T, Ogando NS, Leijs AA, Urakova N, Mark BL, Snijder EJ, Myeni SK,
948 Kikkert M. 2024. Deubiquitinating activity of SARS-CoV-2 papain-like protease does not
949 influence virus replication or innate immune responses in vivo. PLOS Pathogens
950 20:e1012100.
951 74. van der Meer Y, van Tol H, Krijnse Locker J, Snijder Eric J. 1998. ORF1a-Encoded Replicase
952 Subunits Are Involved in the Membrane Association of the Arterivirus Replication Complex.
953 Journal of Virology 72:6689-6698.
954 75. Widjaja I, Wang C, van Haperen R, Gutiérrez-Álvarez J, van Dieren B, Okba NMA, Raj VS, Li W,
955 Fernandez-Delgado R, Grosveld F, van Kuppeveld FJM, Haagmans BL, Enjuanes L, Drabek D,
956 Bosch BJ. 2019. Towards a solution to MERS: protective human monoclonal antibodies
957 targeting different domains and functions of the MERS-coronavirus spike glycoprotein.
958 Emerg Microbes Infect 8:516-530.
959 76. de Wilde AH, Raj VS, Oudshoorn D, Bestebroer TM, van Nieuwkoop S, Limpens R, Posthuma
960 CC, van der Meer Y, Bárcena M, Haagmans BL, Snijder EJ, van den Hoogen BG. 2013. MERS-
961 coronavirus replication induces severe in vitro cytopathology and is strongly inhibited by
962 cyclosporin A or interferon-α treatment. J Gen Virol 94:1749-1760.

77. Su B, Bettcher LF, Hsieh W-Y, Hornburg D, Pearson MJ, Blomberg N, Giera M, Snyder MP, Raftery D, Bensinger SJ, Williams KJ. 2021. A DMS Shotgun Lipidomics Workflow Application to Facilitate High-Throughput, Comprehensive Lipidomics. Journal of the American Society for Mass Spectrometry 32:2655-2663.
78. Ghorasaini M, Mohammed Y, Adamski J, Bettcher L, Bowden JA, Cabruja M, Contrepois K, Ellenberger M, Gajera B, Haid M, Hornburg D, Hunter C, Jones CM, Klein T, Mayboroda O, Mirzaian M, Moaddel R, Ferrucci L, Lovett J, Nazir K, Pearson M, Ubhi BK, Raftery D, Riols F, Sayers R, Sijbrands EJG, Snyder MP, Su B, Velagapudi V, Williams KJ, de Rijke YB, Giera M. 2021. Cross-Laboratory Standardization of Preclinical Lipidomics Using Differential Mobility Spectrometry and Multiple Reaction Monitoring. Analytical Chemistry 93:16369-16378.
79. Faas FG, Avramut MC, van den Berg BM, Mommaas AM, Koster AJ, Ravelli RB. 2012. Virtual nanoscopy: generation of ultra-large high resolution electron microscopy maps. J Cell Biol 198:457-69.

Figure legends

Figure 1

Gene expression of host factors of the DNL pathway increases upon MERS-CoV infection. A) Schematic representation of the main steps of the *de novo* lipogenesis pathway, the key enzymes involved (ACLY, ACC, FASN), and the downstream biological functions of the resulting fatty acids. Double arrows indicate that multiple reactions are involved, but not depicted here. Small-molecule inhibitors used in this study are denoted in red. PTMs: posttranslational modifications. Schematic created using Biorender.com B) Gene expression analysis of key host factors participating in DNL and phospholipid synthesis (dark gray) or fatty acid oxidation (light gray) in mock-infected Huh7 cells in comparison with MERS-CoV-infected cells (MOI 5) at 12 h p.i. The mRNA levels of *ACLY*, *ACC*, *FASN*, *SCD-1*, *DGAT1*, *ADRP*, *CPT1a* and *ACOX* were determined by RT-qPCR and normalized against the mock-infected control. Data are represented as mean ± SD of two biological replicates. Statistical significance was calculated using two-way ANOVA and applying Bonferroni multiple comparison correction, * $p<0.05$, ** $p< 0.01$, *** $p< 0.001$, **** $p< 0.0001$.

Figure 2

DNL inhibition strongly reduces the release of infectious MERS-CoV progeny, without affecting intracellular viral RNA synthesis. A) Huh7 cells or B) MRC5 were infected with MERS-CoV (MOI 5) and treated with either DMSO (vehicle control) or 10 μM TOFA from 1 h p.i. onward. Cell lysates were harvested at 12 h p.i. (Huh7 cells) or 16 h p.i. respectively, and intracellular viral RNA copies were measured by RT-qPCR. C) and D) Infectious viral progeny was quantified by plaque assay on Huh7 cells, using the harvested culture supernatant (see panel A and B, respectively). E) Huh7 cells were infected with MERS-CoV (MOI 5) and treated with either DMSO (vehicle control) or 15 μM TVB-2640 from 1 h p.i. onward. At 16 h p.i., cells were harvested, and intracellular viral RNA copies were measured by RT-qPCR. F) Infectious viral progeny from TVB-2640-treated and untreated Huh7 cells (see panel E) was quantified by plaque assay on Huh7 cells. G) Huh7 cells were infected with MERS-CoV (MOI 5) and treated with either DMSO (vehicle control) or 10 μM TOFA from 1 h p.i. onward. Samples were collected at 12, 14, and 16 h p.i. Infectious viral progeny was quantified by plaque assay on Huh7 cells. While at 12 h p.i the number of infectious virus particles was below the detection limit of the assay, virus titers increased over time at 14 h p.i and 16 h p.i. H) Analysis of the secretory pathway's functionality upon TOFA treatment. Huh7 cells were transfected with a plasmid expressing *Gaussia* luciferase, a naturally secreted reporter protein. From 8 h post transfection., transfected cells were treated with either 10 μM TOFA or 5 μM Brefeldin A. At 24 h post compound addition, the levels of extracellular *Gaussia* luciferase secreted in the supernatant were measured using an enzymatic assay (see Materials and Methods). I) The cell monolayers from the same wells (panel H) were also lysed and intracellular *Gaussia* luciferase expression was measured and compared with the amount of secreted reporter protein. Dotted lines indicate the

background levels measured. Data are represented as mean ± SD of two (D), three (B, E, G) or four (H, I) biological replicates. Statistical significance was calculated using one-way ANOVA and applying Bonferroni multiple comparison correction, *** $p < 0.001$

Figure 3

TOFA treatment induces pronounced changes in the cellular lipidomic profile of mock- and MERS-CoV-infected cells. Huh7 cells were treated with DMSO or 10 μM TOFA. The amounts of intracellular lipids were determined by mass spectrometry at 12 h after compound addition. The graphs show different classes of lipids and their relative abundance compared to the total lipidome. A) triglycerides (TG), cholesterol esters (CE), diacylglycerol (DG), free fatty acids (FFAs). Data are represented as mean ± SD of three biological replicates. Statistical significance was calculated using unpaired Student's t-test, where * $p<0.05$, ** $p< 0.01$, *** $p< 0.001$, **** $p< 0.0001$. B) Huh7 cells were infected with MERS-CoV (MOI 5) and treated with either DMSO (vehicle control) or 10 μM TOFA from 1 h p.i. onward. Samples were collected at 9 and 12 h p.i. The medium was removed, cells were washed and fixed. The next day the fixed cells were stained with BODIPY 493/503 (lipid droplets), and Hoechst 33342 (nuclei) and the presence of lipid droplets was analyzed by wide field fluorescence microscopy.

Figure 4

Subcellular localization of MERS-CoV envelope proteins following TOFA treatment**.** Huh7 cells were infected with MERS-CoV, treated with TOFA as previously described, fixed at 12 h p.i and analyzed using immunofluorescence microscopy.

Cells were triple-labelled for A) S and E proteins or B) S and M proteins in combination with labeling for giantin, as a marker for the Golgi complex. Confocal images are representative of at least two independent biological replicates. White arrows point to co-localization foci of two or three markers.

Figure 5

Effect of TOFA treatment on MERS-CoV structural protein expression and post-translational modifications. Expression levels of S protein (using separate antibodies against the S1 and S2 subunits), N protein, M protein, and E protein were analyzed by western blot, using β-actin as internal control. A) Huh7 cells were infected with MERS-CoV and treated with DMSO or TOFA as previously described. Supernatants were collected at 16 h p.i. and progeny virus particles were pelleted through a sucrose cushion by ultracentrifugation, lysed, and used for Western blot analysis. B) Huh7 cells were infected with MERS-CoV and DMSO- or TOFA-treated as previously described, and samples were collected at 9 and 12 h p.i. for analysis by Western blotting. C) Western blot for PNGase assay (described in Materials and Methods) using lysates collected from MERS-CoV-infected Huh7 cells and collected at 12 h p.i. Blots are representative of at least two independent biological replicates.

Figure 6

TEM analysis of TOFA-treated Huh7 cells infected with MERS-CoV. Cells were infected with MOI 5, treated with TOFA or with DMSO and, at 12 h p.i, fixed and processed for electron microscopy. A) Morphologically comparable virus-induced DMVs (asterisks) can be readily observed in both conditions. Close-ups of the boxed areas are provided in the insets. B) Extracellular virions abundantly present in the

extracellular space of DMSO-treated MERS-CoV-infected cells (i, inset: zoomed-in image of the boxed area), but not in the extracellular space of TOFA-treated and virus-infected cells (ii). C) Consecutive stages of MERS-CoV particle assembly in DMSO-treated and infected cells are represented; assembly events were split in two categories for simplicity (see Materials and Methods), denoted as early-stage assembly events of budding nucleocapsid complexes in membranes of the secretory pathway (panels i and ii) and late-stage assembly events including nearly fully-formed virus particles and virions fully-budded inside large vesicles (iii). D) In TOFA-treated MERS-CoV-infected cells early assembly stage events, which are represented in panels (i) and (ii), were abnormally abundant, revealing a stalling of virus particle assembly in the presence of the compound. Mitochondria are annotated with M, convoluted membranes with CM, and cell nuclei with N. Scale bar is 200 nm.

Figure 7

Exogenous palmitic acid supplementation partially rescues MERS-CoV assembly after TOFA treatment. A) Alignment of partial S and E protein C-terminal sequences from selected coronaviruses using the following accession numbers: MERS-CoV (NC_019843), SARS-CoV (NC_004718) SARS-CoV-2 (NC_045512), MHV (AY700211), TGEV (AJ271965), IBV (NC_001451), HCoV-229E (NC_001451). Cysteines next to the transmembrane domain that can serve as palmitoylation substrates are highlighted in yellow and noted with an asterisk. B) Huh7 cells were infected with MERS-CoV (MOI 5) and treated with either DMSO (vehicle control) or 30 μM 2-BP from 1 h p.i. onward. At 16 h p.i., cell lysates were harvested, and intracellular viral RNA copies were measured by RT-qPCR. C) Infectious viral

progeny was quantified by plaque assay on Huh7 cells. Data are represented as mean ± SD of three independent experiments. D) Huh7 cells were infected with MERS-CoV (MOI 5) and treated from 1 h p.i. onward with DMSO supplemented with 100 μM BSA, TOFA, TOFA supplemented with 100 μM BSA-PA, or TOFA supplemented with 100 μM BSA-OA. At 16 h p.i., samples were collected, and infectious viral progeny was quantified by plaque assay on Huh7 cells. Data are represented as mean ± SD of two independent experiments. Statistical significance was calculated using one-way ANOVA and applying Dunnet multiple comparison correction, **** $p< 0.0001$ and ** $p< 0.01$, ns: not significant. E) Huh7 cells were infected with MERS-CoV and treated with DMSO, TOFA or TOFA with BSA-PA from 1 h p.i. onward as previously described, and samples were collected at 12 h p.i. for analysis by western blotting. Blots are representative of at least two independent biological replicates. F-I) Huh7 cells were infected with MERS-CoV and treated as described above. At 12 h p.i., samples were fixed and processed for TEM. F) Post addition of palmitic acid, the number of extracellular virus particles present in TOFA-treated virus-infected cells is increased. G) Virions either in the late-stage (advanced/ fully assembled particles) or early-stage were quantified manually (see Materials and Methods), and the ratio of both classes was determined. H) Number of DMVs per μm^2 of cytoplasm determined manually (see Materials and Methods) in the DMSO supplemented with 100 μM BSA-treated, TOFA-treated or TOFA and BSA-PA-treated virus-infected cells. I) In the same samples, the area of CMs (in nm^2) was also determined per μm^2 of cytoplasm (see Materials and Methods). Data are represented as mean ± SD of three separate stiches. Statistical significance was calculated using one-way ANOVA and applying Tukey multiple comparison correction, *** $p< 0.001$, ** $p< 0.01$, and * $p<0.05$.

Supplementary data 1

Western blot analysis of ACC and FASN in MERS-CoV-infected Huh7 cells, at 9 h and 12 h p.i.

Supplementary data 2

Cytotoxicity graphs. Cell viability following treatment with various small-molecule inhibitors used in this study was evaluated in different cell lines using the MTS assay at 24 h post compound treatment. Viability was normalized against the DMSO control. A) TOFA in Huh7 cells, B) TVB-2640 in Huh7 cells, C) 2-BP in Huh7 cells, D) TOFA in MRC5 cells, E) palmitic acid-BSA in Huh7 cells, F) oleic acid-BSA in Huh7 cells.

Supplementary data 3

Changes in the cellular lipidomic profile upon inhibition of ACC. Huh7 cells were treated with DMSO or TOFA. The amounts of intracellular lipids were determined by mass spectrometry 12 h after compound addition. Different classes of lipids and their relative abundance compared to the total lipidome are depicted in the graphs. A) phosphatidylcholine lipids (PC), phosphatidylserine (PS), phosphatidylethanolamine (PE), Lyso-PC, Lyso-PE, sphingomyelins (SM), phosphatidylinositides (PI), phosphatidylglycerides (PG), phosphatidic acids (PA), ceramides (Cer d18:0), Cer 18:1, lactosyl-CER (LacCER), hexosyl-ceramides. Data are represented as mean ± SD of three biological replicates. Statistical significance was calculated using unpaired Student's t-test, where * $p<0.05$, ** $p< 0.01$, *** $p< 0.001$, **** $p< 0.0001$, B-C) Huh7 cells were treated as described above and 12h post treatment medium was

removed, the cells were washed and incubated with BODIPY 493/503 for 1 h. Cells were then fixed, the nuclei were stained with Hoechst 33342 and the presence of lipid droplets was analyzed by confocal microscopy. Representative microscopy images of two independent biological replicates are depicted.

Supplementary data 4

Uncropped images used for Figure 4. Boxed areas represent the enlarged regions used in Figure 4.

Supplementary data 5

Subcellular localization of MERS-CoV structural proteins in the presence of TOFA**.** Huh7 cells were infected with MERS-CoV and treated with TOFA as previously described and fixed at 12 h p.i. Cells were labelled simultaneously for S and M or S and E proteins in combination with a marker for PDI or ERGIC, resulting in a triple labelling. Confocal images are representative of at least two independent biological replicates.

Supplementary data 6

Full blots used for Figure 5.

Supplementary data 7

Full blots for Figure 7.

Supplementary data 8

Immunofluorescence analysis of MERS-CoV-infected (MOI 5) Huh7 cells, DMSO- or TOFA-treated, 12 h p.i. Cells were labelled for the N protein (green) and dsRNA (red).

Figure 1

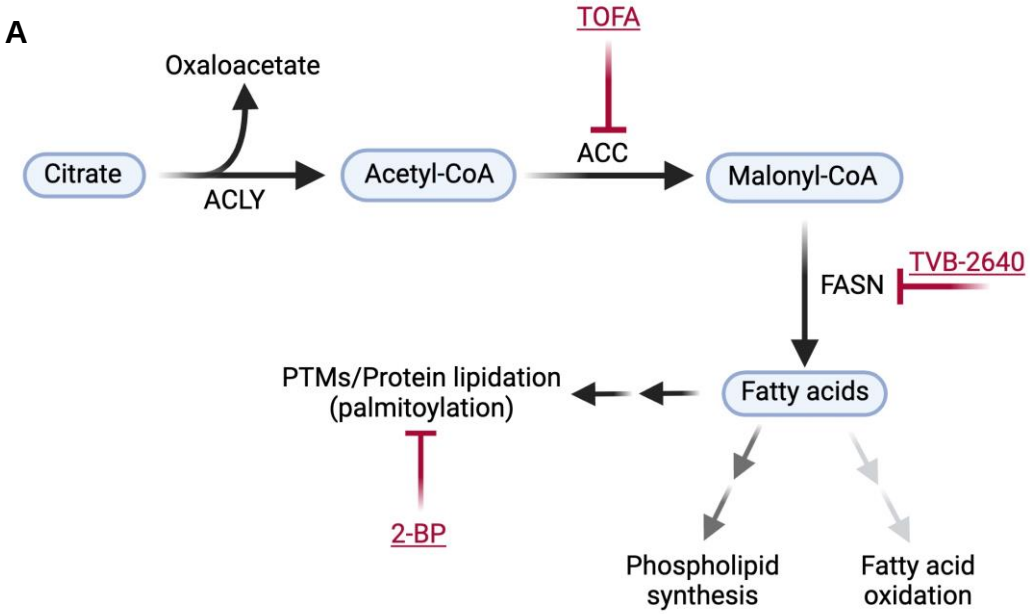
A
TOFA
Oxaloacetate
Citrate
ACLY
Acetyl-CoA
ACC
Malonyl-CoA
FASN
TVB-2640
PTMs/Protein lipidation
(palmitoylation)
Fatty acids
2-BP
Phospholipid
synthesis
Fatty acid
oxidation

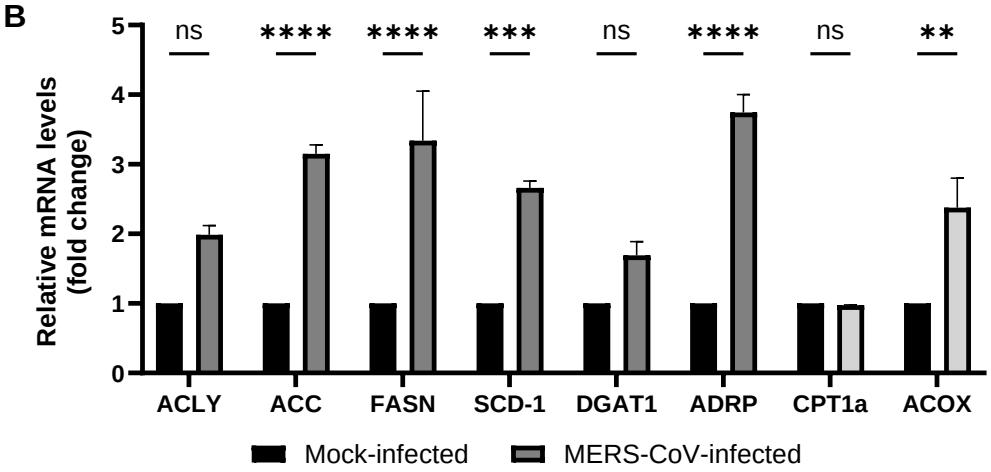
B
Relative mRNA levels
(fold change)
0
1
2
3
4
5
ns
****
****
***
ns
****
ns
**
ACLY
ACC
FASN
SCD-1
DGAT1
ADRP
CPT1a
ACOX
Mock-infected
MERS-CoV-infected

Figure 2

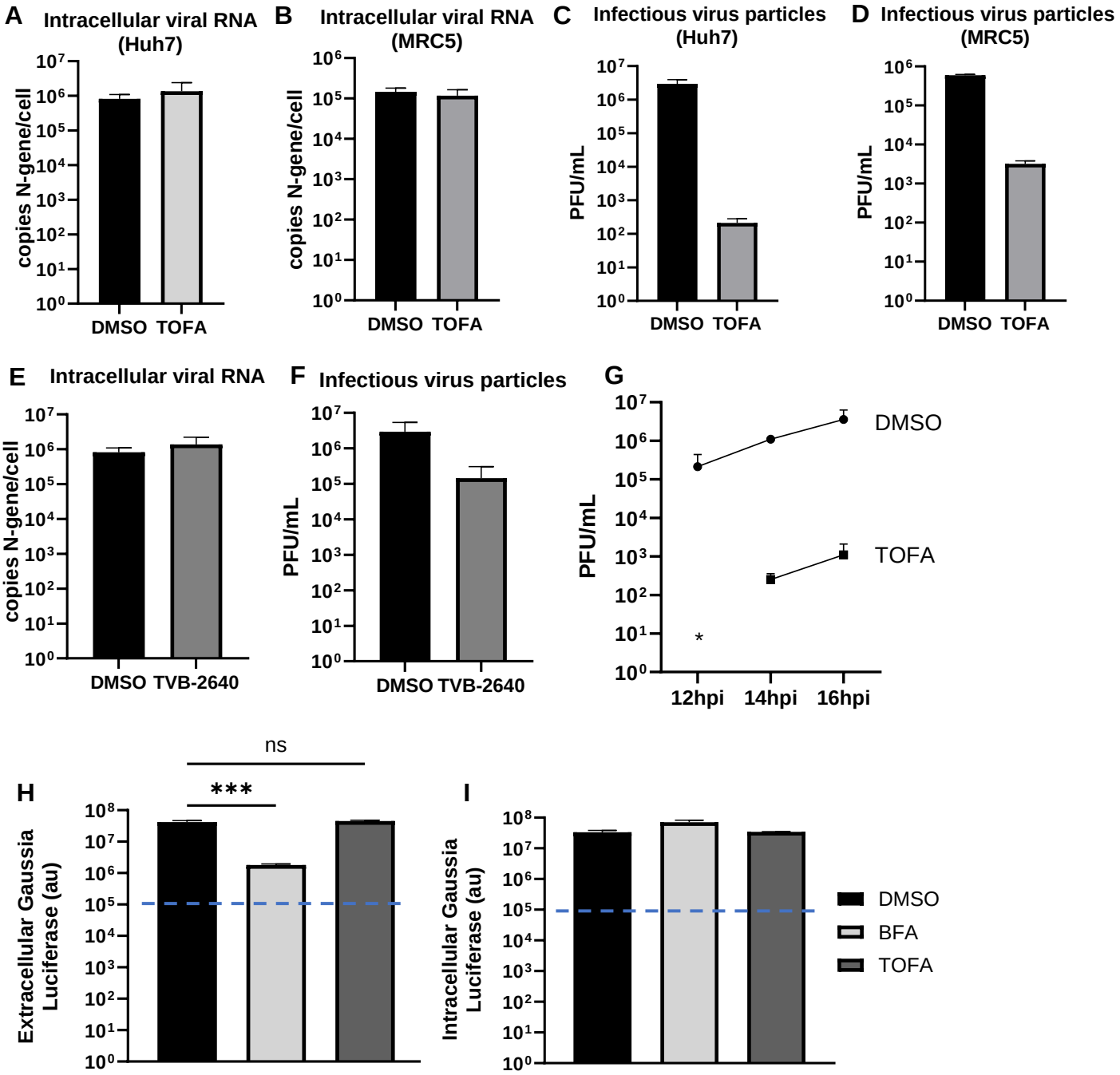
A
Intracellular viral RNA (Huh7)
copies N-gene/cell
DMSO
TOFA
B
Intracellular viral RNA (MRC5)
copies N-gene/cell
DMSO
TOFA
C
Infectious virus particles (Huh7)
PFU/mL
DMSO
TOFA
D
Infectious virus particles (MRC5)
PFU/mL
DMSO
TOFA
E
Intracellular viral RNA
copies N-gene/cell
DMSO
TVB-2640
F
Infectious virus particles
PFU/mL
DMSO
TVB-2640
G
PFU/mL
DMSO
TOFA
*
12hpi
14hpi
16hpi
ns
***
H
Extracellular Gaussia Luciferase (au)
I
Intracellular Gaussia Luciferase (au)
DMSO
BFA
TOFA

Figure 3

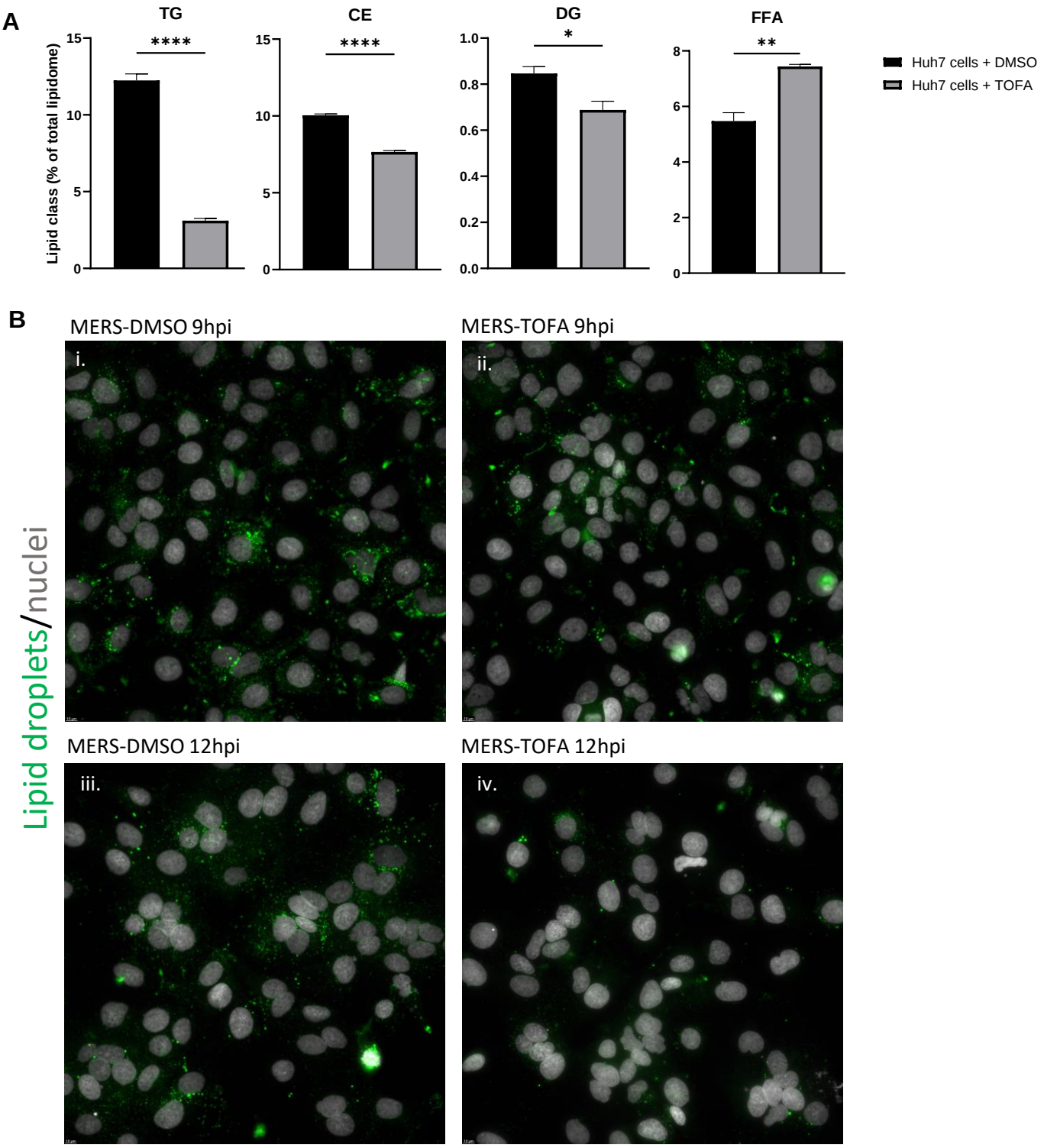
A
TG
CE
DG
FFA
Lipid class (% of total lipidome)
****
****
*
**
Huh7 cells + DMSO
Huh7 cells + TOFA
B
MERS-DMSO 9hpi
MERS-TOFA 9hpi
MERS-DMSO 12hpi
MERS-TOFA 12hpi
i.
ii.
iii.
iv.
Lipid droplets/nuclei

Figure 4

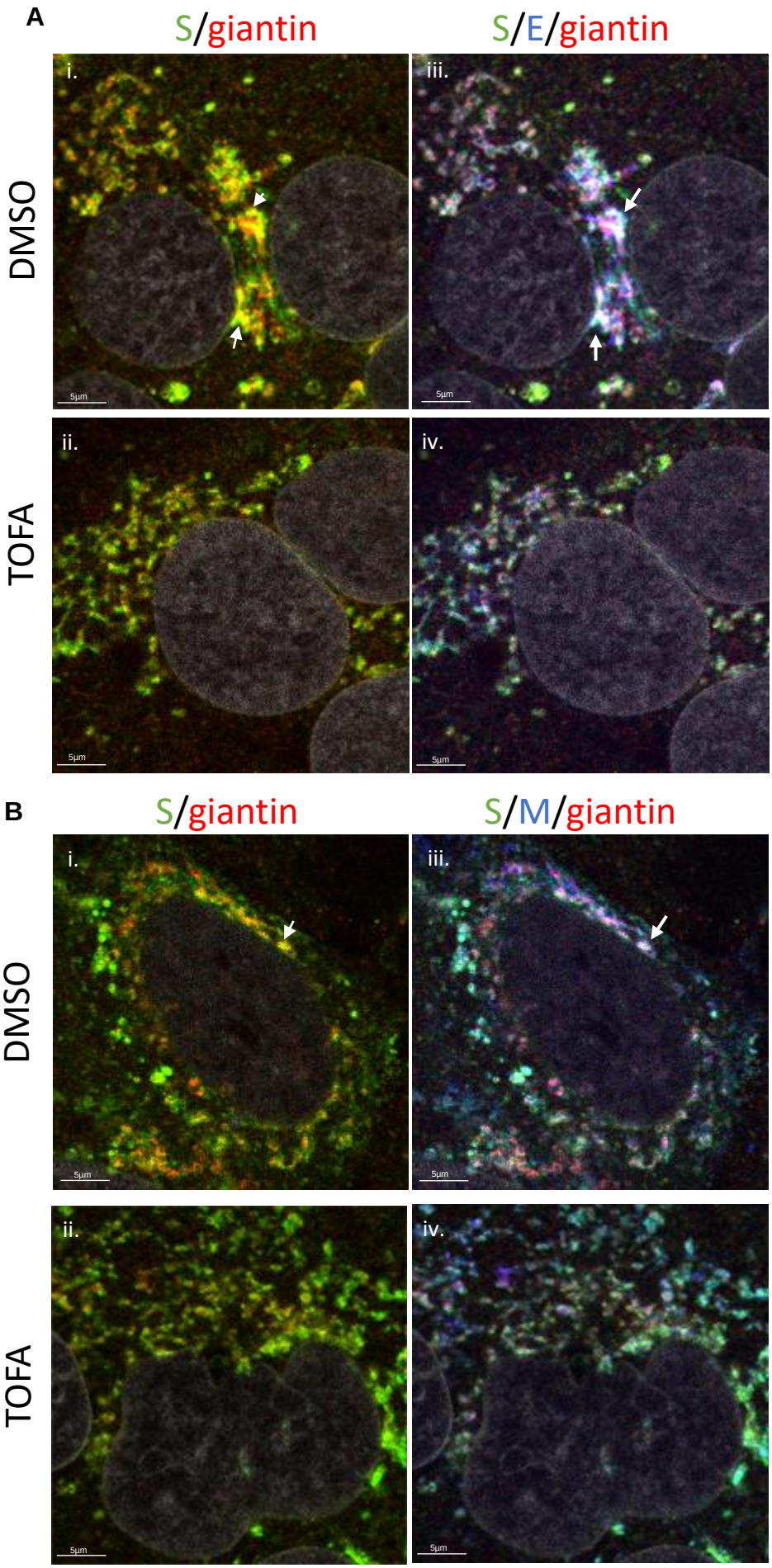
A
S/giantin
S/E/giantin
DMSO
TOFA
i.
iii.
ii.
iv.
5µm
B
S/giantin
S/M/giantin
DMSO
TOFA
i.
iii.
ii.
iv.
5µm

Figure 5

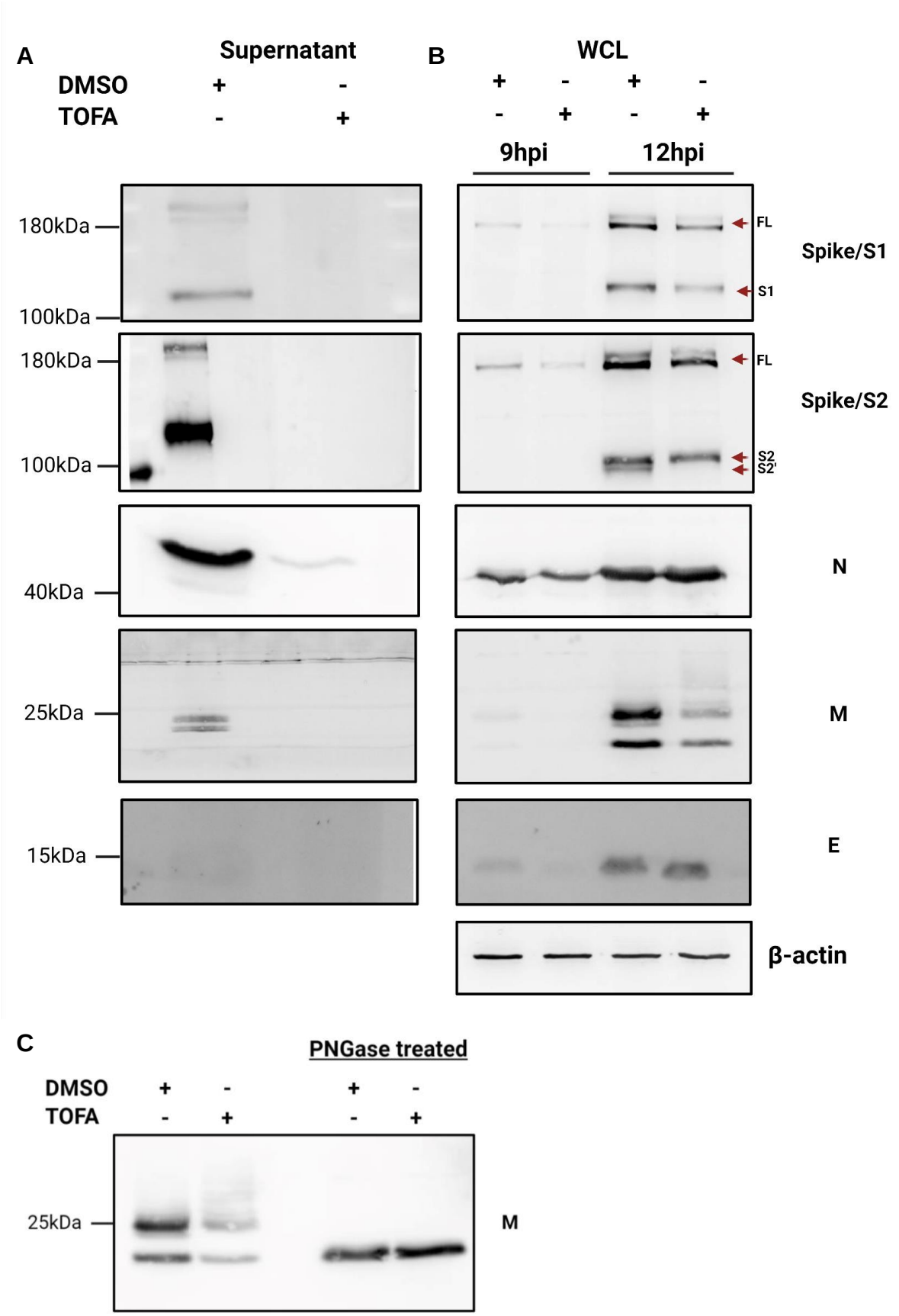
A
Supernatant
DMSO + -
TOFA - +
180kDa
100kDa
180kDa
100kDa
40kDa
25kDa
15kDa
B
WCL
+ - + -
- + - +
9hpi
12hpi
FL
S1
Spike/S1
FL
S2
S2'
Spike/S2
N
M
E
β-actin
C
PNGase treated
DMSO + - + -
TOFA - + - +
25kDa
M

Figure 6

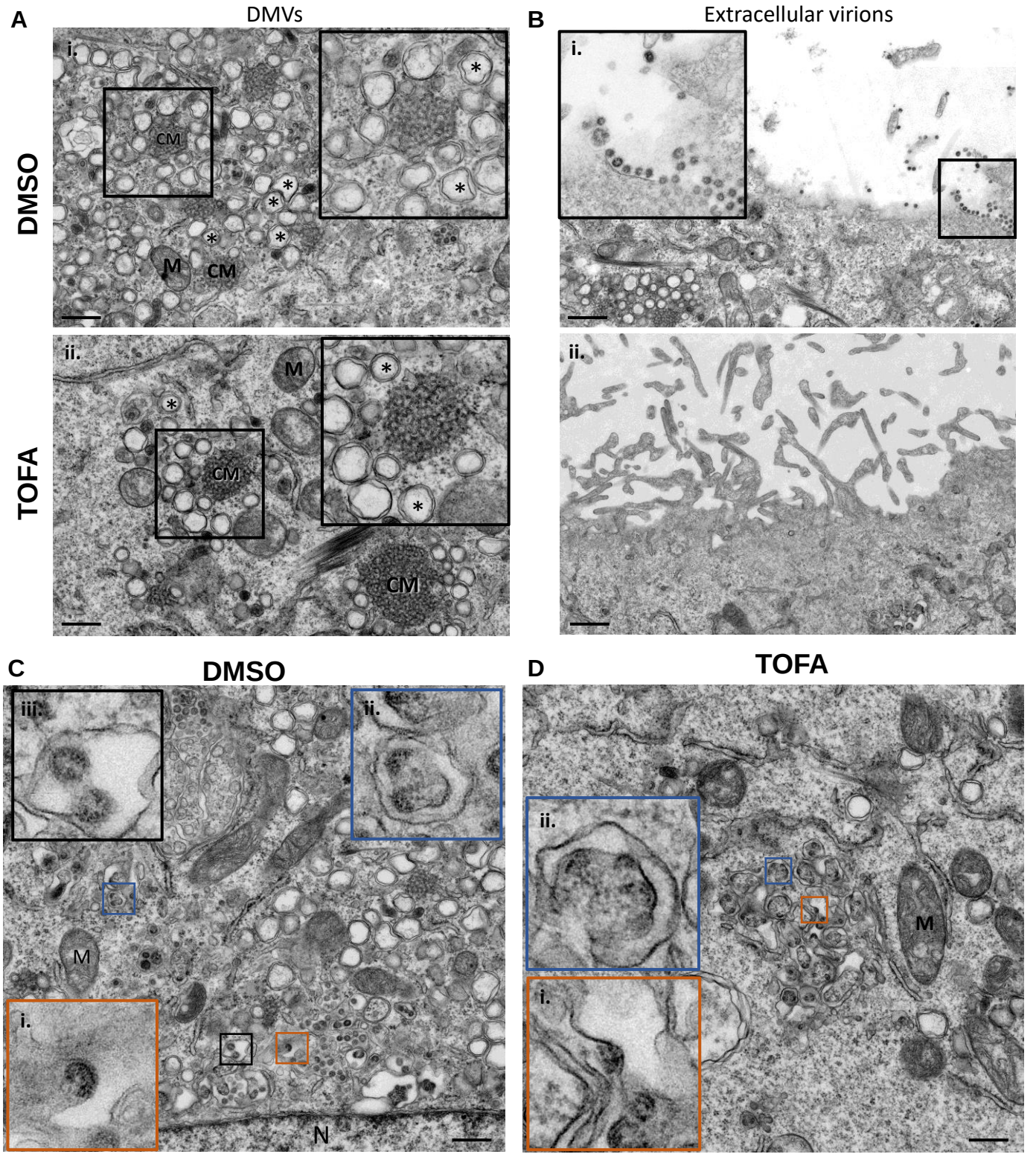
A
DMVs
B
Extracellular virions
DMSO
TOFA
i.
ii.
CM
M
C
DMSO
D
TOFA
iii.
N

Figure 7

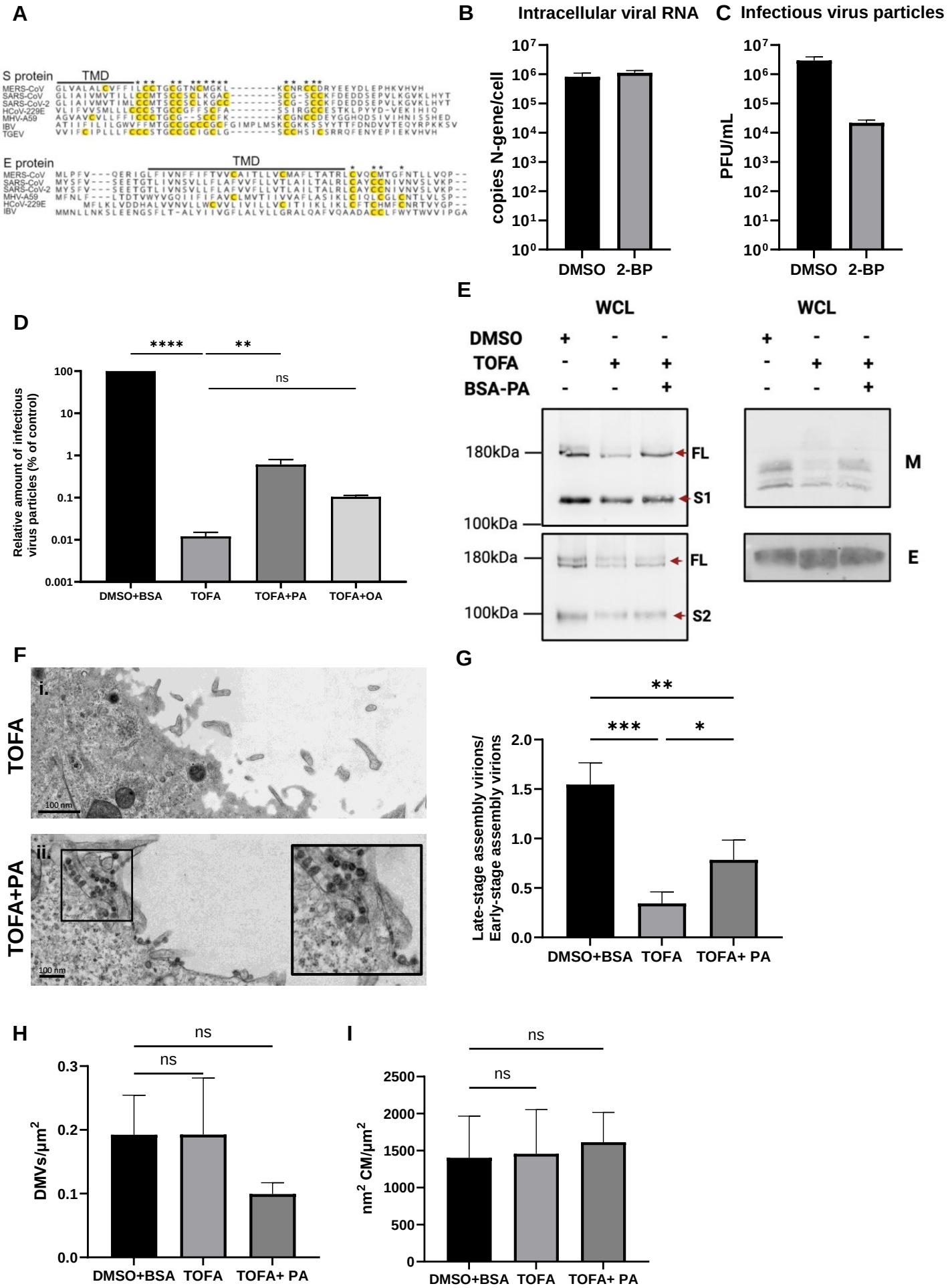
A
S protein
TMD
MERS-CoV
SARS-CoV
SARS-CoV-2
HCoV-229E
MHV-A59
IBV
TGEV
E protein
TMD
MERS-CoV
SARS-CoV
SARS-CoV-2
MHV-A59
HCoV-229E
IBV
B
Intracellular viral RNA
copies N-gene/cell
DMSO
2-BP
C
Infectious virus particles
PFU/mL
DMSO
2-BP
D
****
**
ns
Relative amount of infectious virus particles (% of control)
DMSO+BSA
TOFA
TOFA+PA
TOFA+OA
E
WCL
WCL
DMSO
TOFA
BSA-PA
180kDa
100kDa
FL
S1
M
FL
S2
E
F
TOFA
TOFA+PA
i.
ii.
100 nm
100 nm
G
**
***
*
Late-stage assembly virions/ Early-stage assembly virions
DMSO+BSA
TOFA
TOFA+ PA
H
ns
ns
DMVs/µm²
DMSO+BSA
TOFA
TOFA+ PA
I
ns
ns
nm² CM/µm²
DMSO+BSA
TOFA
TOFA+ PA

Figure S1

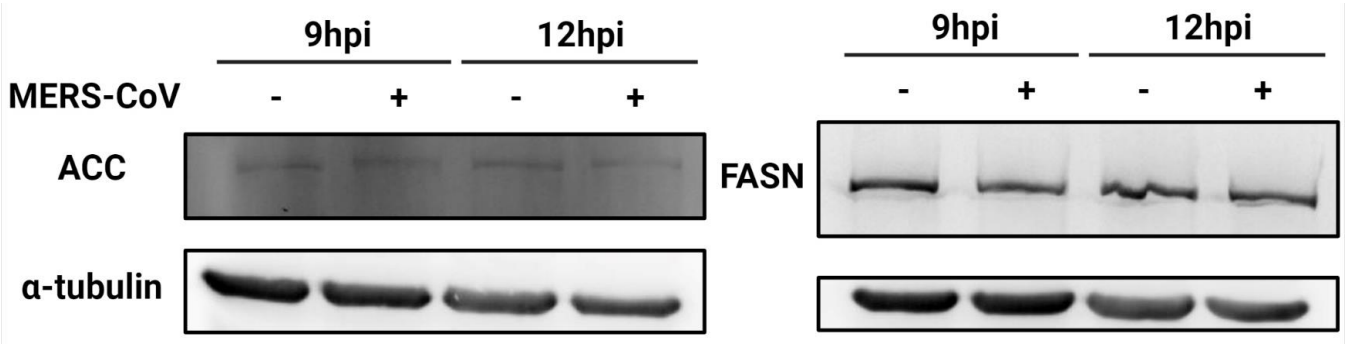

Full blots

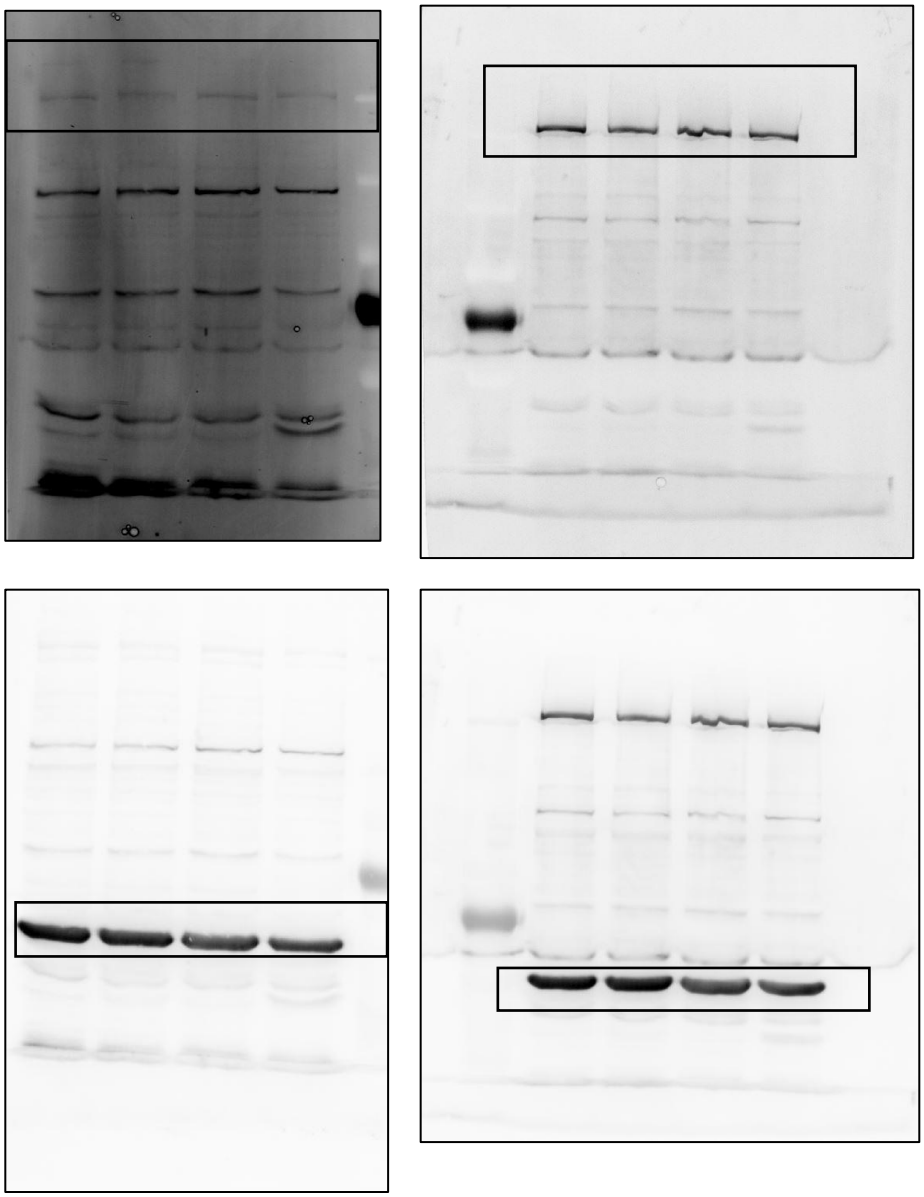

Figure S2

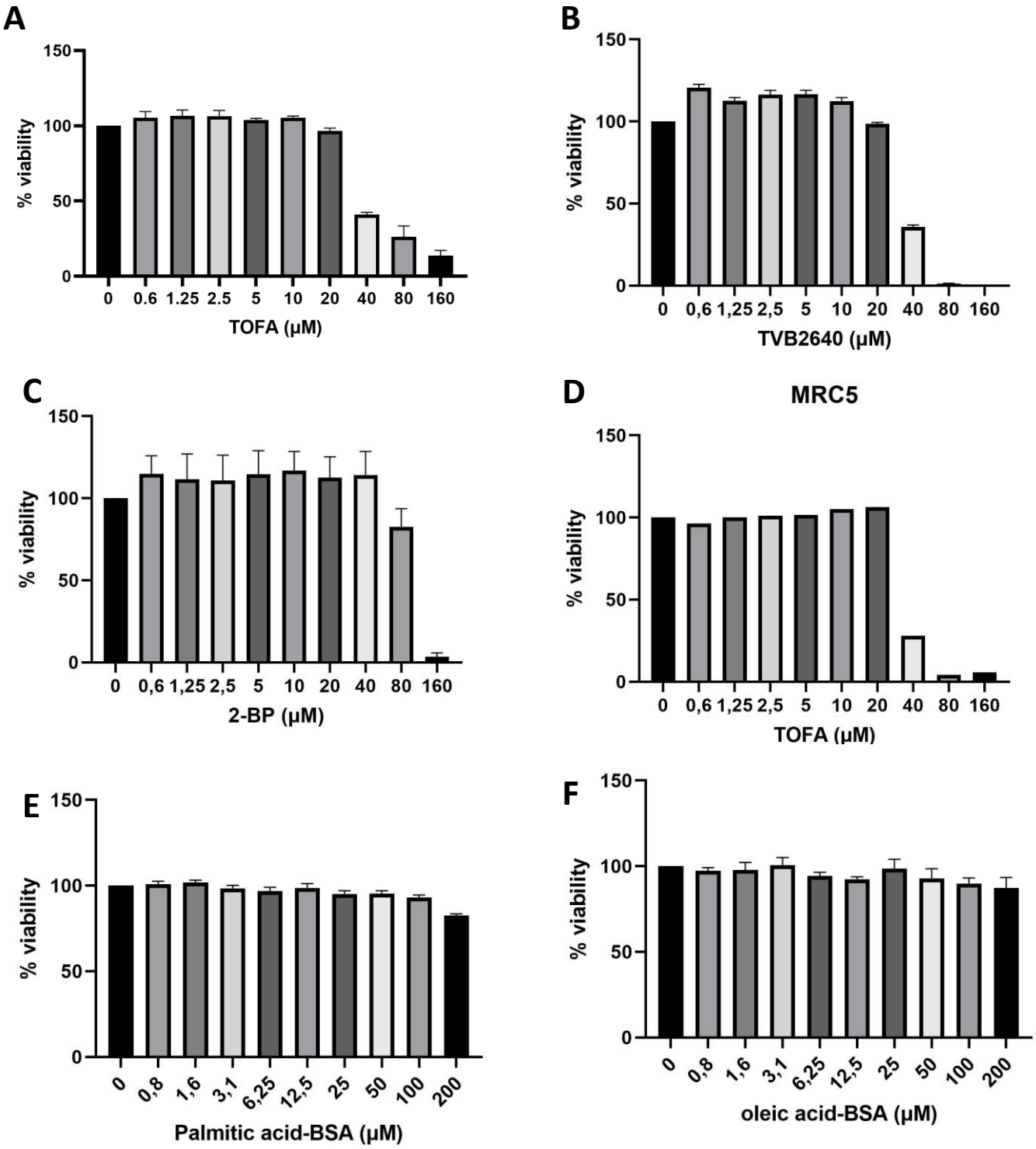
A
% viability
150
100
50
0
0 0.6 1.25 2.5 5 10 20 40 80 160
TOFA (µM)
B
% viability
150
100
50
0
0 0,6 1,25 2,5 5 10 20 40 80 160
TVB2640 (µM)
C
% viability
150
100
50
0
0 0,6 1,25 2,5 5 10 20 40 80 160
2-BP (µM)
D
MRC5
% viability
150
100
50
0
0 0,6 1,25 2,5 5 10 20 40 80 160
TOFA (µM)
E
% viability
150
100
50
0
0 0,8 1,6 3,1 6,25 12,5 25 50 100 200
Palmitic acid-BSA (µM)
F
% viability
150
100
50
0
0 0,8 1,6 3,1 6,25 12,5 25 50 100 200
oleic acid-BSA (µM)

Figure S3

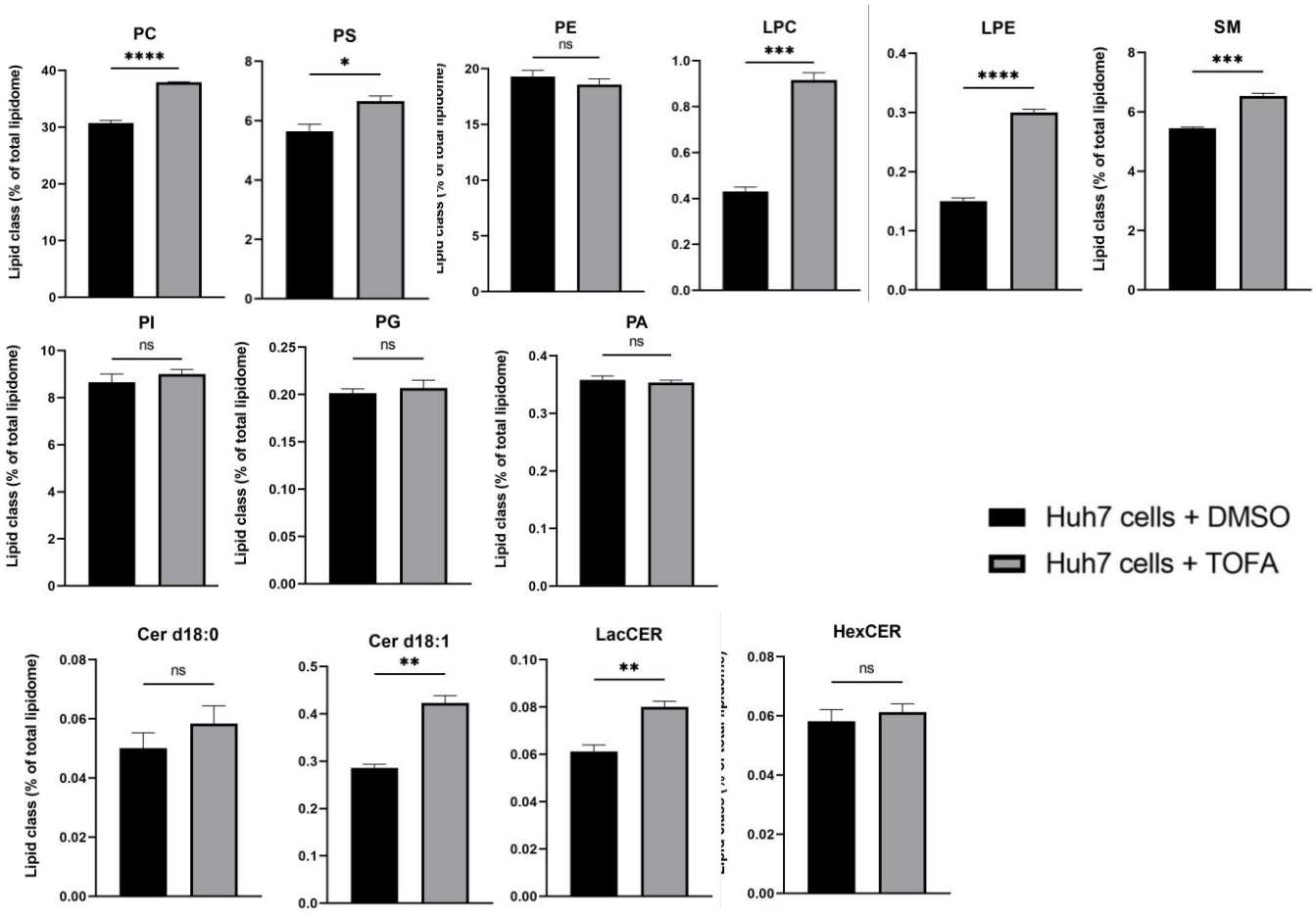
PC
****
PS
*
PE
ns
LPC
***
LPE
****
SM
***
PI
ns
PG
ns
PA
ns
Cer d18:0
ns
Cer d18:1
**
LacCER
**
HexCER
ns
Lipid class (% of total lipidome)
Huh7 cells + DMSO
Huh7 cells + TOFA

B

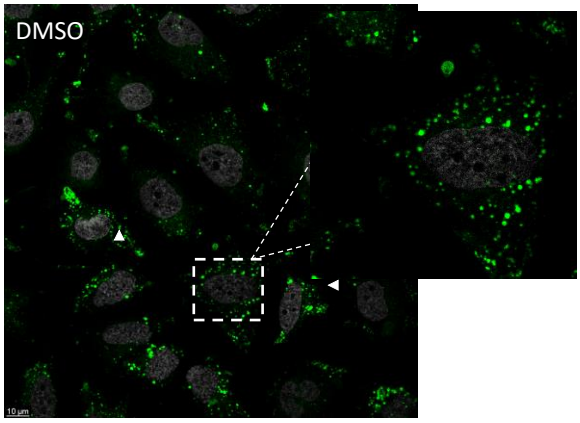
DMSO

C

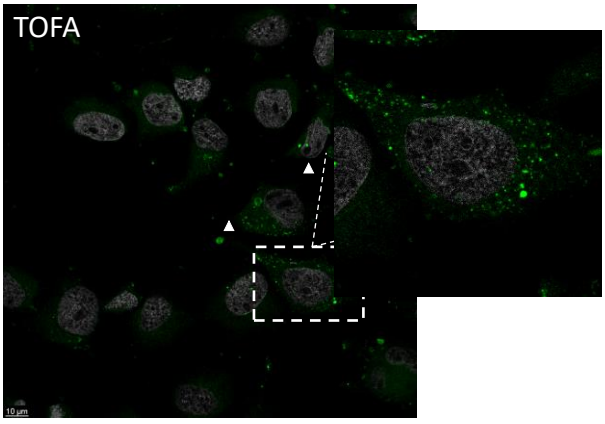
TOFA

Figure S4 for Figure 4

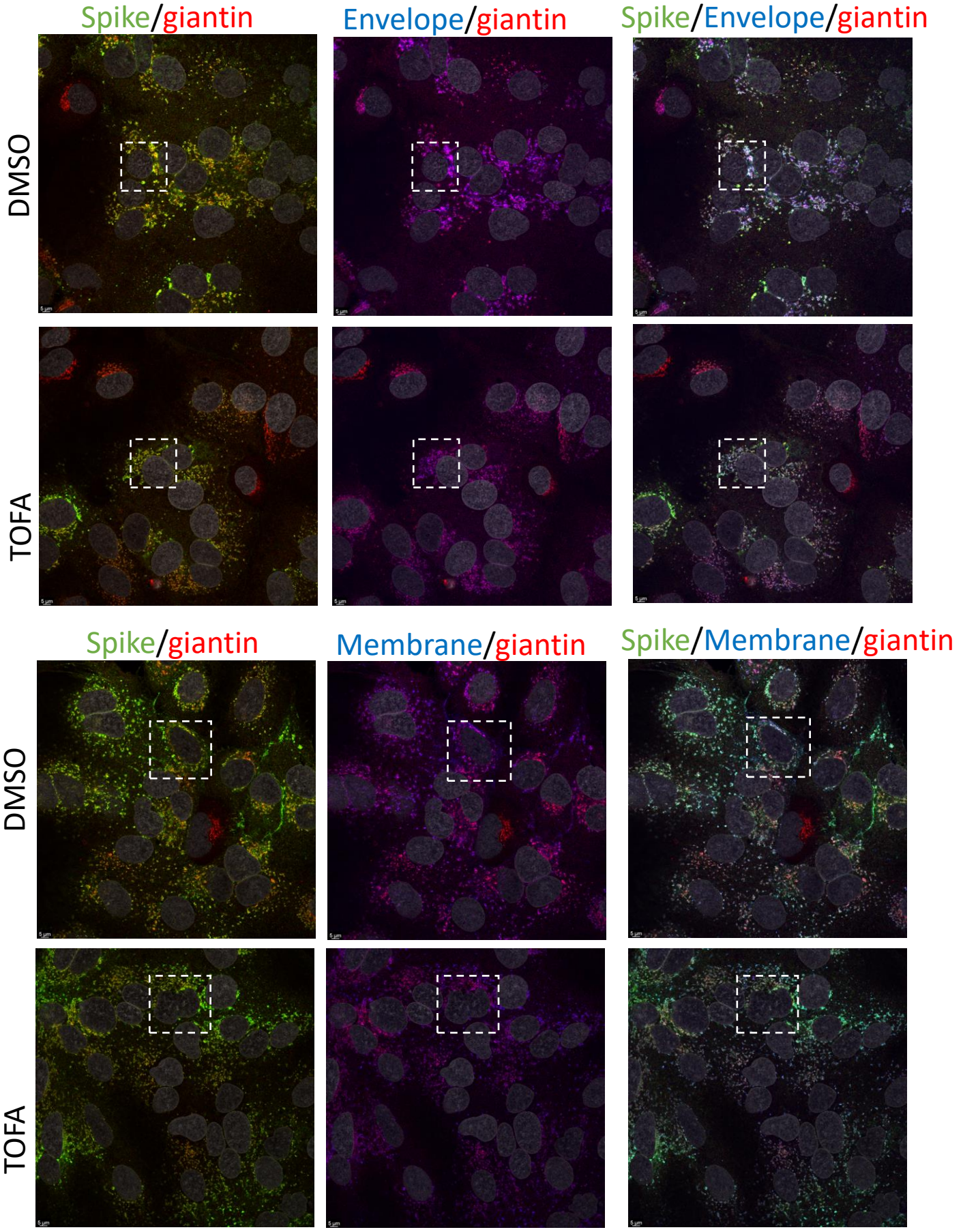

Figure S5

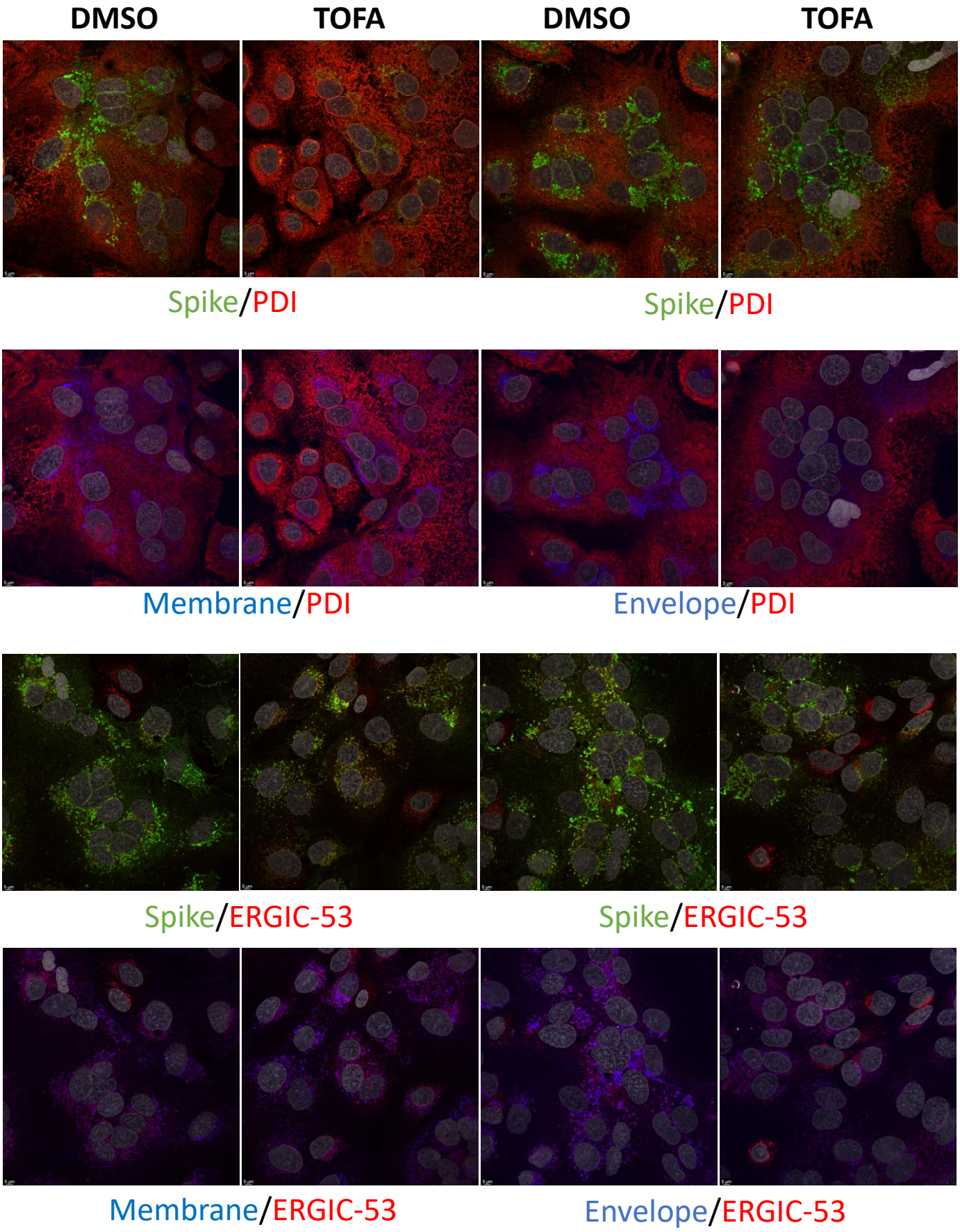
DMSO
TOFA
DMSO
TOFA
Spike/PDI
Spike/PDI
Membrane/PDI
Envelope/PDI
Spike/ERGIC-53
Spike/ERGIC-53
Membrane/ERGIC-53
Envelope/ERGIC-53

Figure S6

Full Blots for Figure 5

S1 (SN)

S2 (SN)

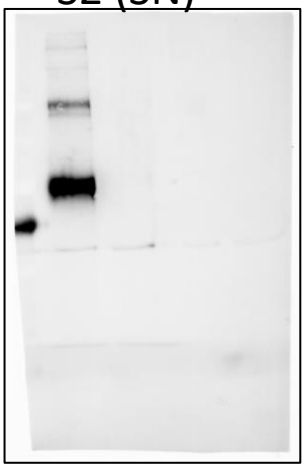

N (SN)

M (SN)

S1 (WCL)

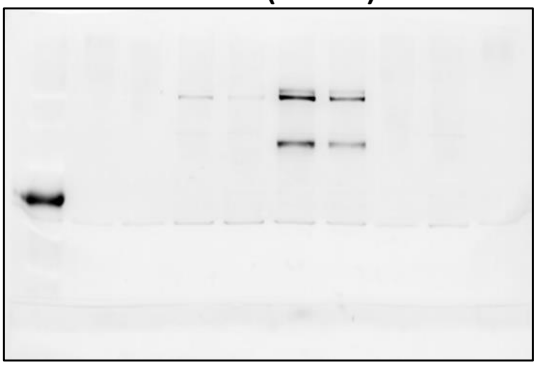

E (WCL) E (SN)

S2 (WCL)

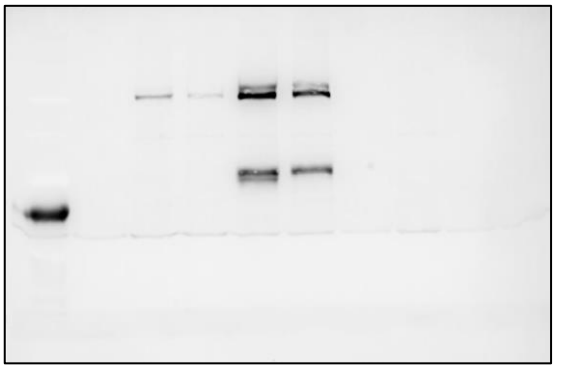

M (WCL) and beta-actin

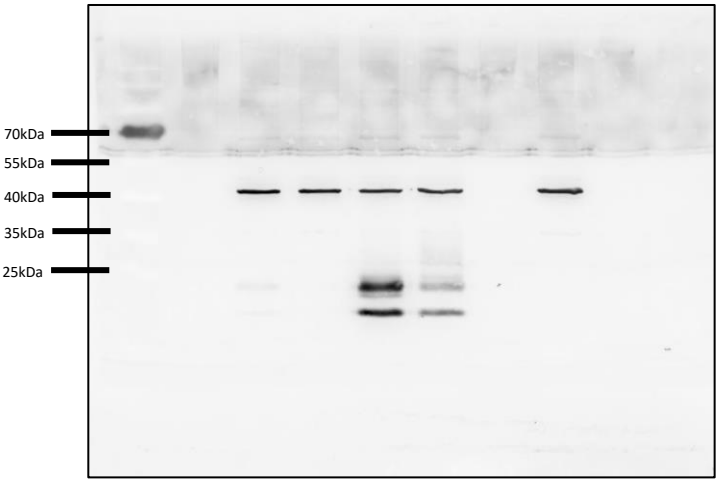

N (WCL)

Figure S7

Full blots for Figure 7

S1

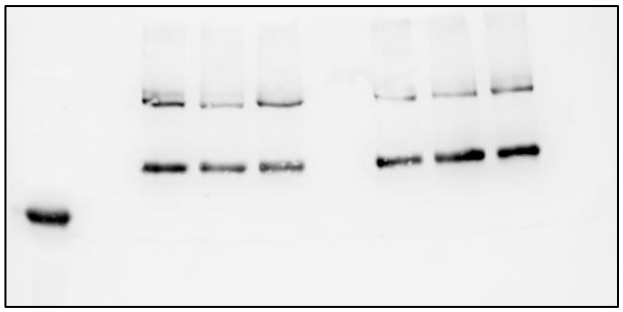

S2

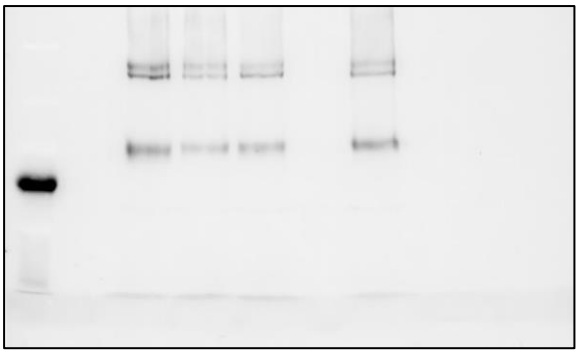

N

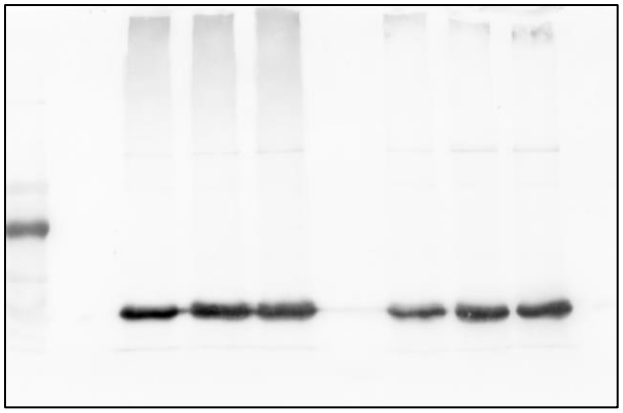

E

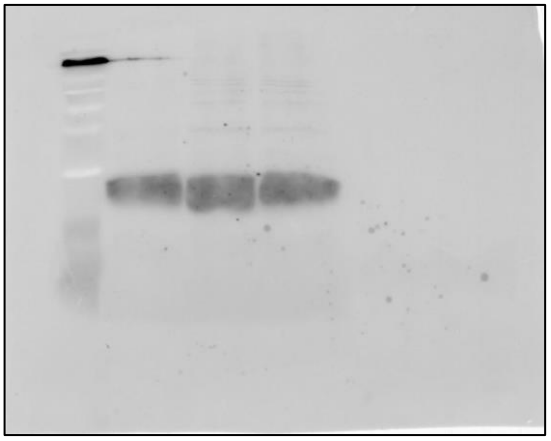

M

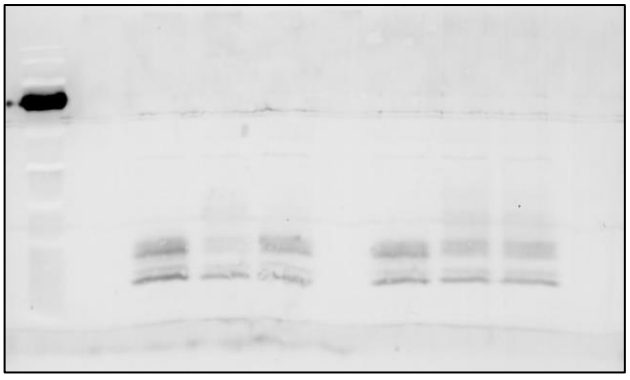
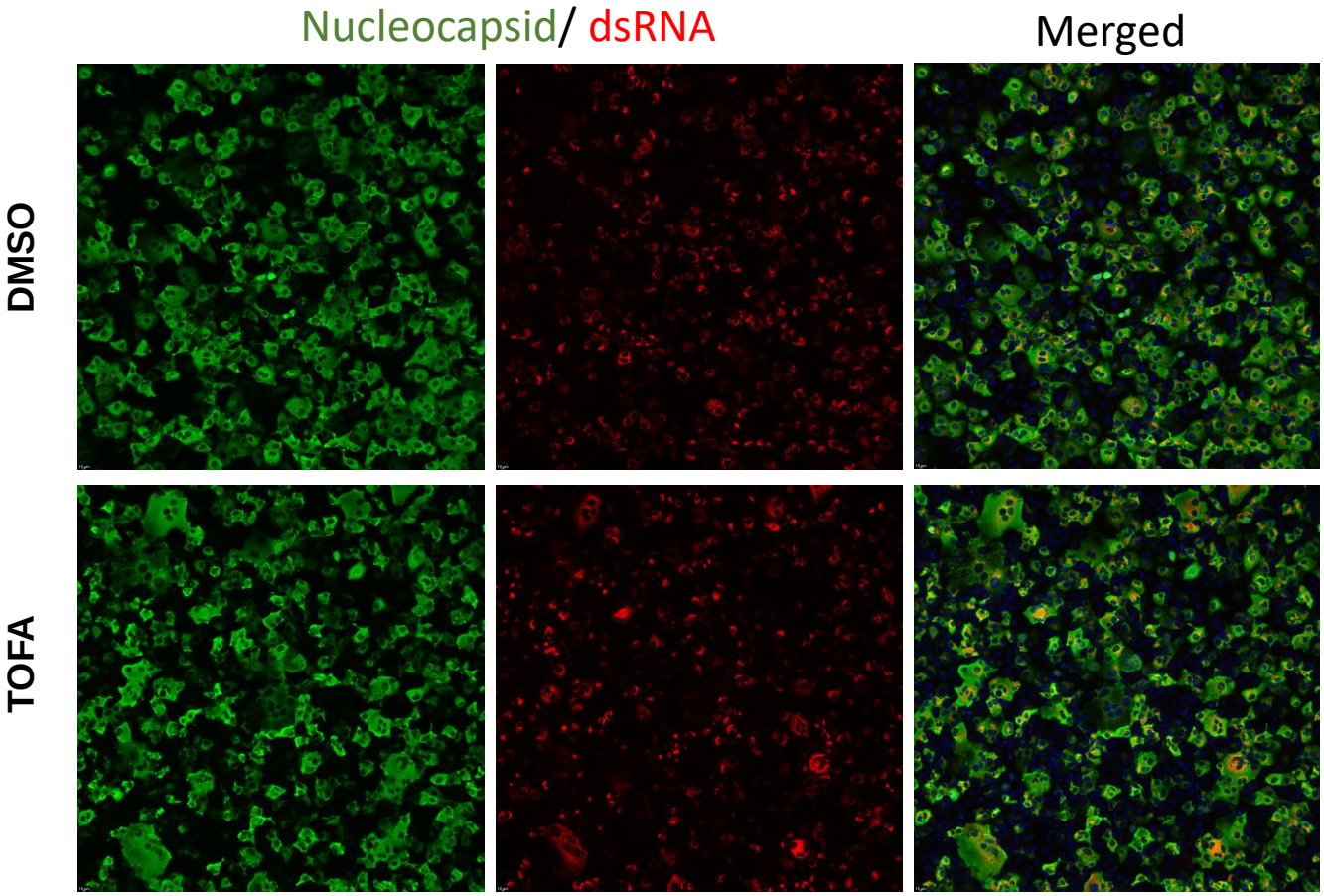
Figure S8